Research Square

Preprints are preliminary reports that have not undergone peer review.
They should not be considered conclusive, used to inform clinical practice,
or referenced by the media as validated information.

Parkin-dependent ubiquitination of TAX1BP1 directs efficient autophagic removal of defective mitochondria.

Philipp Kahle

philipp.kahle@uni-tuebingen.de

Eberhard Karls University of Tuebingen, Hertie Institute for Clinical Brain Research
https://orcid.org/0000-0002-8587-1731

Anna Lechado-Terradas

Eberhard Karls University of Tuebingen

Bianca Lemke

Eberhard Karls University of Tuebingen

Katharina Zittlau

Eberhard Karls University of Tuebingen

Boris Macek

University of Tuebingen https://orcid.org/0000-0002-1206-2458

Article

Keywords:

Posted Date: September 21st, 2026

DOI: https://doi.org/10.21203/rs.3.rs-6512400/v1

License: This work is licensed under a Creative Commons Attribution 4.0 International License.
Read Full License

Additional Declarations: There is **NO** Competing Interest.

Parkin-dependent ubiquitination of TAX1BP1 directs efficient autophagic removal of defective mitochondria

Anna Lechado-Terradas[1], Bianca Lemke[2], Katharina I. Zittlau[2], Boris Macek[2], Philipp J. Kahle[1, 3]

[1]Laboratory of Functional Neurogenetics, Department of Neurodegeneration, Hertie Institute for Clinical Brain Research and German Center for Neurodegenerative Diseases, Faculty of Medicine, University of Tübingen, Germany.
[2]Quantitative Proteomics Group, Department of Biology, Interfaculty Institute of Cell Biology, University of Tübingen, Germany.
[3]Department of Biochemistry, Faculty of Science, University of Tübingen, Germany.

Abstract

In stressed cells, the recessive Parkinson's disease (PD) gene products phosphatase and tensin homolog induced kinase 1 (PINK1) and parkin (PRKN) mediate the autophagic removal of damaged mitochondria (mitophagy). Upon mitochondrial membrane potential disruption, PINK1 phosphorylation activates the ubiquitin ligase parkin which ubiquitinates various mitochondrial protein substrates. These feed-forward modifications on the mitochondria surface eventually attract ubiquitin-binding autophagy adaptors that target ubiquitinated mitochondria to autophagosomes and indirectly contribute to autophagosome formation. Investigating post-translational protein modifications during this process, we detected transient ubiquitination of K549 within the third coiled-coil domain (CC3) of Tax1 binding protein 1 (TAX1BP1) in HeLa cells expressing wild-type but not catalytically inactive parkin. Parkin-dependent ubiquitination did not target TAX1BP1 to proteasomal degradation but rather appeared as a regulatory modification. In cells with the full complement of autophagy adaptors, TAX1BP1 plays only a minor role in mitophagy. However, when expressed as a sole autophagy adaptor, both wild-type and ubiquitination deficient TAX1BP1 were capable of promoting parkin-dependent mitophagy, albeit mitochondria degradation was slightly delayed under mutant conditions. Use of the lysosomal inhibitor bafilomycin A indicated classical autophagolysosomal targeting of damaged mitochondria mediated by wild-type TAX1BP1. However, for the ubiquitination-deficient TAX1BP1 under the same conditions, an increased prevalence of enlarged endolysosomal vesicles carrying

accumulated TAX1BP-positive autophagosomes filled with mitochondrial material became significantly apparent. Thus, while ubiquitination of the CC3 domain of TAX1BP1 is not essential for complete removal of damaged mitochondria, the lack of CC3 in TAX1BP1 reroutes the flux of parkin-dependent mitophagy to a less efficient endolysosmal degradative pathway. Interestingly, the PD gene product VPS35, becomes prominently engaged in this alternative mitophagy pathway.

Introduction

Mitochondrial quality control and turnover are essential for cellular homeostasis. Cellular stress associated with mitochondrial membrane depolarization induces a pathway leading to removal of damaged mitochondria that is activated by the two most common recessive Parkinson's disease (PD) gene products, phosphatase and tensin homolog induced kinase 1 (PINK1) and parkin (PRKN) (Geisler *et al.*, 2010; Matsuda *et al.*, 2010; Narendra, Jin, *et al.*, 2010; Narendra, Kane, *et al.*, 2010). Under basal conditions, the nuclear encoded PINK1 protein is efficiently imported into mitochondria, where it is rapidly degraded. Upon dissipation of the mitochondrial membrane potential, PINK1 lacks the driving force for mitochondrial import and hence accumulates on the mitochondrial outer membrane (OMM). There, the PINK1 kinase domain faces the cytosol to phosphorylate ubiquitin and the ubiquitin-like domain of parkin, a process which activates the ubiquitin ligase parkin recruited to the OMM of depolarized mitochondria (Kondapalli *et al.*, 2012; Shiba-Fukushima *et al.*, 2012; Koyano *et al.*, 2014; Ordureau *et al.*, 2015). Various ubiquitin linkages target proteins from depolarized mitochondria to proteasomal and autophagic degradation (Lechado-Terradas *et al.*, 2022). Five major autophagy adaptors have been implicated to connect ubiquitinated mitophagy cargo with the autophagy machinery, including p62 sequestosome-1 (p62/SQSTM), optineurin (OPTN), nuclear dot protein of 52kDa (NDP52), next to breast cancer type 1 susceptibility gene 1 protein (NBR1), and Tax-1 binding protein 1 (TAX1BP1) (Geisler *et al.*, 2010; Heo *et al.*, 2015; Lazarou *et al.*, 2015; Richter *et al.*, 2016). These autophagy adaptors do not statically bridge ubiquitinated mitophagy cargo with microtubule-associated protein 1 light chain 3 (LC3)-containing phagophore membranes, but dynamic post-translational modifications (PTMs) are critical modulators of their function and contribute to the recruitment of autophagy-related proteins involved in autophagosome biogenesis (i.e: ATG9 vesicles, uncoordinated protein 51-like kinase (ULK1) complex) (Yamano *et al.*, 2020, 2024; Turco *et al.*, 2021; Nguyen *et al.*, 2023). For example, phosphorylation by tumor necrosis factor receptor associated nuclear factor kB activator

binding kinase 1 (TBK1) contributes to important regulatory dynamics of OPTN and NDP52 for selective autophagic removal of damaged mitochondria (Heo *et al.*, 2015; Richter *et al.*, 2016; Yamano *et al.*, 2024).

Investigating the phospho-proteome and ubiquitylome throughout the time course of mitophagy in active parkin expressing HeLa cells (Zittlau *et al.*, 2022), we detected transient ubiquitination of TAX1BP1 at K549 within the third coiled-coil domain (CC3) of this autophagy adaptor. Validation of TAX1BP1 ubiquitination in cells expressing catalytically active (WT) or a ligase-dead parkin mutant (C431A), confirmed parkin-dependent ubiquitination of the autophagy adaptor at early stages of mitophagy. Removal of the highly ubiquitinated CC3 domain of TAX1BP1 reduced TAX1BP1 distribution on mitochondrial material and induced the engulfment of accumulated autophagosomes into enlarged endolysosomal vesicles (potential amphisomes), apparently rerouting the mitophagy pathway to the endolysosomal system. Thus, the ubiquitinatable CC3 of TAX1BP1 directs depolarized mitochondrial material to autophagosomal degradation, whereas CC3 perturbation mediates the degradation of accumulated autophagosomes with damaged mitochondrial cargo through a less efficient pathway involving endolysosomal trafficking into enlarged endolysosomes. Interestingly, the PD gene product VPS35 became prominently engaged in the alternative mitophagy pathway described in this study, clearly recognizing the surroundings of the identified enlarged degradative vesicles.

Results

Transient ubiquitination of TAX1BP1 in Parkin-dependent mitophagy

Examining the ubiquitylome of HeLa cells stably expressing parkin treated with the mitochondrial uncoupler carbonyl cyanide m-chlorophenylhydrazone (CCCP) (Zittlau *et al.*, 2022), we detected transient ubiquitination of TAX1BP1 at K549 (Figure 1A, B). The ubiquitination-indicating di-glycine motifs were detected by mass spectrometry predominantly for TAX1BP1 peptides containing K549, with only minor signals for K571, also located in the CC3 region, and K439, upstream of CC3 (Figure 1A, B). TAX1BP1 ubiquitination only occurred in cells expressing wild-type (WT) parkin, but not catalytically inactive C431A-parkin (Figure 1B). Other studies previously reported K549-TAX1BP1 to be increasingly ubiquitinated in a parkin-dependent manner and following a similar time course as the one described here (Rose *et al.*, 2016). Validation of parkin-dependent ubiquitination of TAX1BP1 via Western blotting confirmed the differences between WT- and C431A-parkin

observed in the mass-spectrometry screen (Figure 1B, C). In HeLa cells stably expressing active parkin, but not ligase-inactive C431A-parkin, CCCP treatment caused a band shift compatible with TAX1BP1 poly-ubiquitination peaking around 4h after mitochondrial membrane depolarization. TAX1BP1 ubiquitination vanished at later time points of mitophagy, when parkin substrates like translocase of outer membrane 20kDa subunit (TOM20) and voltage-dependent anion channel (VDAC) were degraded (Figure 1C). Overall, TAX1BP1 levels decreased parallelly to VDAC and TOM20 degradation during early depolarization (2-4 h CCCP) but increased after extended depolarization (8-18 h CCCP), indicating that early steps of mitophagy might also involve some degradation of the autophagy adaptor along with mitochondrial cargo.

As early stages of PINK1/parkin mitophagy rely on proteasomal degradation of immediate-early parkin substrates, we hypothesized that the identified ubiquitinated TAX1BP1 could target the autophagy adaptor for early proteasomal degradation. In order to test this, HeLa cells stably expressing parkin were transfected with TAX1BP1 and subjected to mitophagy in the presence or absence of the proteasomal inhibitor MG132 (Figure S1). Endogenous TAX1BP1 was not reduced after short depolarization (2h CCCP) while a slight reduction of overexpressed TAX1BP1 levels was observed at this early timepoint (Figure S1). Importantly, proteasome inhibition did not stabilize poly-ubiquitinated endogenous or overexpressed TAX1BP1, contrary to what was observed for the known proteasome target MFN1 (Figure S1). Thus, the rapid TAX1BP1 ubiquitination is not part of the initial proteasome-targeting ubiquitination program of OMM-associated proteins at very early stages of mitophagy, but rather appears to be a regulatory PTM of TAX1BP1.

Ubiquitinated TAX1BP1 is enriched in depolarized mitochondria

Mitochondria depolarization triggers the activation of parkin-dependent ubiquitination of mitochondrial proteins that will be recognized by the ubiquitin binding domains of autophagy adaptors for further successful delivery of mitochondrial cargo to autophagosomes (Narendra and Youle, 2024). As expected, endogenous TAX1BP1 translocated to mitochondria after depolarization (Figure 2A). To investigate if the ubiquitinated form of TAX1BP1 was also present on mitochondria, sucrose fractionation experiments were performed. After sucrose fractionation, mitochondrial proteins (i.e: TOM20, VDAC and citrate synthase, CS) were highly enriched in the mitochondria fraction (MTF) (Figure 2B). Under no stress conditions, TAX1BP1 was enriched in the membrane fraction (MMF),

suggesting that TAX1BP1 can localize directly to membranous compartments under basal conditions. However, upon short mitochondrial depolarization, TAX1BP1 was enriched in the MTF, also in the ubiquitinated form (Figure 2B). These data indicate that ubiquitinated TAX1BP1 localizes on depolarized mitochondria where it may contribute to parkin-dependent mitophagy.

Modulation of the ubiquitination pattern of TAX1BP1 has mild effects on the degradation of mitochondrial proteins

TAX1BP1 is one of the autophagy adaptors capable of recognizing ubiquitinated mitochondria and triggering its selective degradation during PINK1/parkin mitophagy (Narendra and Youle, 2024). However, among the identified five selective autophagy adaptors involved in mitophagy, OPTN, NDP52 and TAX1BP1 were characterized as the only ones capable of inducing mitophagy on their own, with TAX1BP1 being the least efficient of the three (Lazarou *et al.*, 2015). Our results are in accordance with the hypothesis of TAX1BP1 having a minor role amongst other autophagy receptors, as siRNA mediated knock-down of TAX1BP1 in WT-parkin HeLa cells did not abolish the degradation of the outer mitochondrial proteins TOM20 and VDAC (Figure S2A). On the other hand, overexpression of TAX1BP1 had a positive effect on mitophagy, as we observed an increased mitochondrial clustering upon short depolarization and TAX1BP1 overexpression (Figure S2B). These results confirm the involvement of TAX1BP1 in parkin-mediated mitophagy and strengthen the notion of TAX1BP1 having a minor role when all other autophagy adaptors are present. Thus, in order to be able to characterize TAX1BP1 functionality isolated in a null autophagy adaptor background, HeLa cells lacking all five major autophagy adaptors were used (from now on, referred as 5KO HeLa) (Lazarou *et al.*, 2015).

Next, in order to understand the relevance of the identified TAX1BP1 ubiquitination events, lysine substitution (K549R) and deletion (ΔCC3) mutants were generated (Figure 3A). Here, 5KO HeLa cells were transiently co-transfected with WT-parkin combined with the indicated TAX1BP1 mutants and mitophagy was induced via CCCP-mediated depolarization at the indicated time-points. Upon co-expression of WT-parkin and WT or K549R-TAX1BP1 after early mitochondrial depolarization (4h CCCP), ubiquitination band shift of TAX1BP1 was observed, even in the absence of all other four complementary autophagy adaptors (Figure 3B). In contrast, ubiquitination was reduced upon expression of ΔCC3-TAX1BP1 under the

same conditions (Figure 3B). This data indicates that most of the TAX1BP1 ubiquitination events observed upon mitochondria depolarization are localized at the CC3 domain of the autophagy adaptor, but are not restricted to K549. In addition, we could confirm a similar ubiquitination phenotype in 5KO HeLa stably expressing WT-parkin (from now on 5KO-PRKN HeLa) (Figure S2C). Here, in addition to a strong ubiquitination reduction for ΔCC3-TAX1BP1, a milder reduction of K549R-TAX1BP1 ubiquitination was observed (Figure S2C). It is important to note that the CC3 of TAX1BP1 is particularly a lysine-rich compared to CC1 or CC2 and that the lysines encoded in the CC3 domain of TAX1BP1 are highly conserved across species [_1](Figure S3). Thus, it is possible that the sole substitution of a single lysine (i.e: K549R) in this domain is not enough to have an impact on the total TAX1BP1 ubiquitination levels, as many other lysines could be alternatively ubiquitinated in this condition.

Next, we focused on the impact of mitochondria turnover upon expression of the different TAX1BP1 mutants. Under control conditions, where neither TAX1BP1 nor parkin were expressed, turnover of TOM20, VDAC, CS and the cytochrome c oxidase subunit 4 isoform 1 (COX4) were not significantly reduced after 4h of CCCP (Figure 3B-C). As expected, upon expression of parkin alone or together with WT-TAX1BP1, an increase in OMM protein degradation was observed (i.e: TOM20 and VDAC) while inner mitochondrial proteins (COX4 and CS) remained unaffected after 4h of CCCP (Figure 3C). These results indicate that the degradation of inner mitochondrial targets requires longer depolarization exposure, consistent with previous studies (Lechado-Terradas *et al.*, 2022; Zittlau *et al.*, 2022). Expression of K549R-TAX1BP1 did not have any impact on TOM20 or VDAC degradation, unlike for ΔCC3-TAX1BP1, which revealed slightly increased TOM20 and ubiquitinated TOM20 levels after 4h CCCP (Figure 3B-C). VDAC turnover was increased upon addition of WT or any TAX1BP1 mutant, when compared to parkin transfection alone. However, changes were found to not be significant, suggesting that the autophagy adaptor may not be required for the elimination of this particular OMM protein (Figure 3C). Overall, these data suggest that abolishing CC3 ubiquitination of TAX1BP1 (ΔCC3-TAX1BP1) delays the autophagy adaptor efficiency on TOM20 degradation.

Modulation of the ubiquitination pattern of TAX1BP1 has mild effects on its translocation behavior to mitochondria

The engulfment of mitochondrial material inside autophagosomes is a step that depends on autophagy adaptor functionality and is regulated at distinct steps: (i) recognition of ubiquitinated mitochondrial proteins, (ii) fostering the recruitment of autophagy effectors, which will initiate autophagosome biogenesis, and (iii) acting as autophagosome tethers through direct interaction with lapidated AT8s at the autophagosome surface, allowing autophagosome packaging. Considering this, we hypothesized that the slight defects observed in mitochondrial degradation could be due to a delay in the TAX1BP1-dependent recognition of mitochondrial material. For this purpose, TAX1BP1 translocation behavior and mitochondria clustering were analyzed.

First, basic immunofluorescence was used to visualize TAX1BP1 translocation on mitochondrial material upon co-expression of WT-parkin (Figure 4A and S4A). Under basal conditions, puncta-like structures were observed for all three TAX1BP1 constructs (Figure S4A). Short mitochondria depolarization induced the translocation of all three TAX1BP1 constructs (Figure 4A), indicating that both K549R- and ΔCC3-TAX1BP1 were capable of recognizing depolarized mitochondria. However, ΔCC3-TAX1BP1 translocation to mitochondria was rather localized in specific regions of the SSBP1 cluster and, unlike parkin translocation, did not co-localize with most of SSBP1 material in some cases (Figure 4A, zoom panel d).

Next, mitochondrial morphology analysis was performed by quantifying mitochondria area after depolarization. In this case, given that matrix protein turnover was not significantly affected after short depolarization (Figure 3C), the matrix protein SSBP1 was used for mitochondrial area quantification by using CellProfiler as previously performed (Sharma *et al*., 2024). Here, after short depolarization and co-expression of Parkin with WT-TAX1BP1, we observed a strong reduction of SSBP1 area when compared to control conditions, indicative of mitochondrial clustering and successful mitophagy (Figure S4B). Importantly, while a reduction of mitochondrial area was also observed with parkin expression only, mitochondrial clustering was not as prominent as when WT-TAX1BP1 was co-expressed (Figure S4B), indicative of delayed or impaired mitophagy in absence of the autophagy adaptor. When analyzing mitochondrial clustering upon co-expression of WT and mutant TAX1BP1, an increase in SSBP1 area and perimeter was observed for ΔCC3-TAX1BP1

while no changes were observed for K549R-TAX1BP1 (Figure 4B-D). These data indicate that ΔCC3-TAX1BP1 shows a delayed efficacy in promoting mitophagy.

Above results seem to indicate that the recognition of depolarized mitochondria is not impaired by any of the mutants, as both K549R- and ΔCC3-TAX1BP1 were co-localizing with mitochondrial material upon depolarization (Figure 4A). However, upon expression of ΔCC3-TAX1BP1 and short depolarization, we observed a delayed degradation of TOM20 (Figure 3B-C) as well as a general delay in mitochondrial clustering, indicated by an increase in SSBP1 foci area and perimeter (Figure 4B-C). Additionally, a partial TAX1BP1 translocation to specific SSBP1 cluster regions was observed (Figure 4A). Thus, we hypothesized that the observed ΔCC3-TAX1BP1 delay in mitophagy progression may be related to TAX1BP1 capability to recognize SSBP1 clusters. For this purpose, the distribution of TAX1BP1 on depolarized mitochondria material was analyzed with CellProfiler. In general, all TAX1BP1 constructs seemed to recognize SSBP1 material in a similar manner, with distribution percentages ranging from 35-45% of SSBP1 area (Figure S4C). While no significant differences were observed between WT and mutant TAX1BP1, a slight reduction of the mitochondrial area recognized by ΔCC3-TAX1BP1 was observed, when compared to WT- and K549R-TAX1BP1 (Figure S4C). To exclude that the observed differences in TAX1BP1 mitochondrial distribution could be due to distinct mitophagy progression stages, parkin distribution on mitochondrial material was additionally analyzed. In this case, no overall differences were observed upon transfection of WT- or mutant TAX1BP1, as parkin-dependent recognition of SSBP1 area was found between 60-65% for all cases (Figure S4D). We additionally monitored the percentage of total TAX1BP1 involved in the recognition of depolarized mitochondria. Here, no differences were observed for WT and mutant TAX1BP1, showing 45-50% of total TAX1BP1 to be engaged with depolarized mitochondria (Figure S4E). We further hypothesized that the differences of TAX1BP1 distribution on SSBP1 foci could be caused by differences in TAX1BP1 capability to translocate to mitochondria. For this purpose, the recognized SSBP1 area (X) was plotted against the percentage of TAX1BP1 translocating to mitochondria (Y) and correlation analysis was performed. Indeed, a significant correlation was observed for WT-TAX1BP1, with increasing TAX1BP1 being able to recognize 40-50% of SSBP1 area, followed by a TAX1BP1 translocation decrease covering up to 60-80% of SSBP1 area (Figure 4E). Correlation analysis was also significant for K549R-TAX1BP1, which behaved similarly as WT but with an increased variability on the percentage of translocated K549R-TAX1BP1 (Y

axis), after reaching a maximum of 70% translocated TAX1BP1 (Figure 4E). Surprisingly, unlike for WT and K549R, no significant correlation was observed for ΔCC3, suggesting an inefficient binding behavior for the deletion mutant unable to recognize more than half of SSBP1 area. Next, to discard that the differences observed could be due to upstream differences in parkin translocation to mitochondria, a similar correlation analysis was applied for parkin mitochondrial translocation (Figure S4F). Here, significant correlation was found in all cases and no drastic differences were observed for parkin translocation upon expression of all TAX1BP1 constructs (Figure S4F). In this case, approximately >80% of SSBP1 was found recognized by parkin (Figure S4F), indicating a comparable parkin translocation and thus a mitophagy progression stage for all three TAX1BP1 expression cases.

Next, to validate the previously observed differences in ΔCC3-TAX1BP1 binding behavior in a context of stable parkin expression, TAX1BP1 mutants were transfected in 5KO-PRKN HeLa cells and TAX1BP1 translocation was analyzed after 4h of CCCP treatment. To confirm mitophagy progression was at an advanced level, only cells with mitochondrial COX4-positive clusters were taken into account. Here, cells were classified based on TAX1BP1 translocation to mitochondria (complete vs. localized distribution) (Figure 4F). Interestingly, a significant increase of cells with localized TAX1BP1 recognition was observed under conditions of K549R- and ΔCC3-TAX1BP1 when compared to WT (Figure 4F). These data indicate that the recognition of depolarized mitochondria is slightly impaired in K549R and ΔCC3-TAX1BP1 (Figure 4E-F).

Blocking autophagy flux in ΔCC3-TAX1BP1 promotes the formation of enlarged TAX1BP1 structures

Next, we sought to examine if the observed differences in mitophagy progression and binding behavior of K549R and ΔCC3 would translate in the capability of the autophagy adaptor to promote complete elimination of mitochondria. For this purpose, mitochondrial degradation after extended depolarization was analyzed in 5KO-PRKN HeLa cells transfected with WT and TAX1BP1 mutants. Interestingly, all TAX1BP1 constructs were able to induce mitochondria degradation after extended CCCP treatment, as an increased number of cells without mitochondria were observed in comparison to control (Figure 5A, 5C). However, when blocking the autophagy flux with bafilomycin A (BafA), we could observe the presence of small and enlarged TAX1BP1-positive puncta co-localizing with the

matrix protein SSBP1 (Figure 5B). Importantly, the percentage of cells harboring enlarged TAX1BP1-positive puncta was significantly higher in ΔCC3-TAX1BP1 compared to WT or K549R (Figure 5D). In addition, TAX1BP1 ubiquitination status at that time-point was validated by means of Western blotting. Here, in accordance to what was observed at an earlier stage of mitophagy (Figure 3B), ubiquitination of TAX1BP1 was conserved upon autophagy flux blockage for WT- and K549R-TAX1BP1 while a strong ubiquitination reduction was seen for ΔCC3 under these conditions (Figure 5E). These data suggests that, while ΔCC3-TAX1BP1 can promote mitochondria elimination as K549R and WT-TAX1BP1 after long depolarization, the degradative mechanisms driven by ΔCC3-TAX1BP1 may differ, as its expression induces a significantly higher prevalence of enlarged TAX1BP1-positive structures carrying mitochondrial material.

Enlarged ΔCC3-TAX1BP1-positive structures are not simple autophagosomes

Given the fact that TAX1BP1 has been considered as the least effective autophagy adaptor to be able to initiate mitophagy in 5KO-HeLa (Lazarou *et al.*, 2015), it was tempting to speculate that the enlarged TAX1BP1/SSBP1-positive identified structures could be indicative of mitochondrial degradation occurring via a distinct autophagy pathway. Thus, several markers were used to investigate the nature of the enlarged TAX1BP1-positive structures carrying mitochondrial material. As BafA is known to inhibit autophagic flux, the first marker to test was the autophagosome marker LC3B. As expected, all small TAX1BP1/HSP60-positive structures were engaged in cup-shaped LC3B-positive rings, suggesting they were indeed autophagosomes (Figure S5A). Also the enlarged TAX1BP1/HSP60-positive structures of WT, K549R and ΔCC3-TAX1BP1 were positive for LC3B (Figure 6A). In all cases, these were composed of multiple LC3B-positive cup-shaped structures across the Z plane, suggesting the enlarged TAX1BP1-positive structures were formed by an accumulation of multiple autophagosomes (Figure 6B).

Later steps of autophagy-mediated degradation rely on the fusion of sealed autophagosomes with lysosomes. However, prior to autophagosome-lysosome fusion, autophagosome maturation takes place and sealed autophagosomes may additionally fuse with endosomes, generating a new degradative vesicles termed amphisome (Zhao, Codogno and Zhang, 2021). Thus, we decided to prove for the following endolysosomal markers: the late endosomal marker RAB7, the member of the retromer complex VPS35 (which is mutated in rare forms of PD) and the late endosomal and marker CD63.

Surprisingly, all large TAX1BP1-positive vesicles carrying mitochondrial material were surrounded by RAB7 and VPS35 signals (Figure 6C-D), indicating that the identified accumulated LC3B/TAX1BP1/HSP60-positive structures were engulfed in large RAB7/VPS35-positive vesicles. Enlarged TAX1BP1-positive vesicles of WT, K549R and ΔCC3 were also positive for CD63 (Figure 6E). These data suggest that the observed TAX1BP1-positive enlarged structures carrying accumulated autophagosomes and further engulfed by vesicles positive for late-endosomal markers, may be the result of impaired autophagosomes and late endosome fusion. However, we cannot discard that the observed enlarged TAX1BP1-positive vesicles are endolysosomes, as BafA treatment does not inhibit the fusion between autophagosomes-lysosomes or autophagosomes-endosomes. On the other hand, the identified small TAX1BP1-positive structures carrying mitochondrial inner material (HSP60 or COX4) were also positive for LC3B and all tested endolysosomal markers, suggesting they were regular mature autophagosomes (Figure S5A-D).

Enlarged ΔCC3-TAX1BP1⁺ vesicles are also observed in parental HeLa cells with all other complementary autophagy adaptors

To confirm the relevance of previously described phenotype in 5KO HeLa, similar experiments were performed in WT-Parkin HeLa cells endogenously expressing all other complementary autophagy adaptors (NDP52, OPTN, NBR1, p62/SQSTM, TAX1BP1) (Figure S6A) (Lazarou *et al*., 2015). Here, siRNA-based transient knockdown experiments were followed by re-transfection of the desired TAX1BP1 constructs and subsequent CCCP-mediated depolarization combined with BafA (Figure 7A). Overall, TAX1BP1 puncta in all conditions colocalized with the mitochondrial marker HSP60 (Figure 7A). Surprisingly, the mean size of all observed TAX1BP1-positive puncta per cell significantly increased upon siRNA knockdown and further TAX1BP1 re-transfection in comparison to controls (Figure 7B). Indeed, when classifying TAX1BP1 puncta size between small (<50 px^2), intermediate (≤150 px^2) or big (> 150 px^2), the majority of TAX1BP1-positive structures were of small or intermediate sizes, while larger puncta represented a much smaller percentage of the total vesicles in all conditions (Figure S6B-C). Of note, there was a 2-fold significant increase of the percentage of larger ΔCC3-TAX1BP1 structures in comparison to WT-TAX1BP1 conditions, reaching 5% of total ΔCC3-TAX1BP1-positive structures identified (Figure 7C). An additional increase of the percentage of larger puncta profiles was observed upon WT-TAX1BP1 transfection when compared to transfection and silencing controls, suggesting the overexpression of TAX1BP1 can increase its vesicle size (Figure 7C). Furthermore, while

the number of cells with large TAX1BP1 puncta was slightly higher in ΔCC3-TAX1BP1 in comparison to re-transfected WT- or K549R-TAX1BP1, the differences were only significant when compared to siRNA controls (Figure 7D). TAX1BP1-positive enlarged structures did also co-localize with mitochondrial matrix and IMM proteins (SSBP1, HSP60 and COX4) in WT-Parkin HeLa (Figure 7A). Next, to relate TAX1BP1 mitochondrial removal efficiency upon expression of the different TAX1BP1 constructs in WT-Parkin HeLa, co-localization analysis of HSP60 and TAX1BP1 was performed. First, the percentage of HSP60 foci co-localizing with TAX1BP1-positive structures of all sizes was analyzed (Figure 7E). An increased percentage of HSP60 co-localizing with TAX1BP1 was observed upon silencing and TAX1BP1 re-transfection in comparison to controls, with no significant differences among all three TAX1BP1 conditions (Figure 7E). These data indicate that all TAX1BP1 constructs enhance the recognition of HSP60 material, in agreement with previous experiments where overexpression of TAX1BP1 had a positive effect on mitochondrial degradation (Figure S2B-C). Next, HSP60 foci co-localizing with enlarged TAX1BP1-positive structures were analyzed (Figure 7F). Here, while there was a slight increase of the percentage of HSP60 foci recognized by enlarged ΔCC3-TAX1BP1-positive structures, no significant differences were found among WT and mutants under silencing conditions (Figure 7F). However, it is worth noting that the mean area of the identified HSP60 foci co-localizing with ΔCC3- and K549R-TAX1BP1 were larger than the ones observed in WT or control conditions, while no differences were observed for WT compared to controls (Figure 7G).

These data indicate that the enlarged ΔCC3-TAX1BP1-positive structures observed in 5KO-PRKN are of dominant nature, despite the partial rescue observed in WT-parkin HeLa, where all complementary autophagy adaptors are present. Overall, we observe an increased prevalence of enlarged ΔCC3 structures capable of recognizing increased amounts of HSP60 in comparison to WT. Similarly, K549R enlarged structures are able to engage with increased amounts of HSP60, however the prevalence of K549R enlarged structures is less abundant than ΔCC3, suggesting a milder phenotype for the site-substitution mutant.

Mass-spectrometry analysis of ΔCC3-TAX1BP1 pulldown reveals defects in intracellular trafficking processes

In order to get an idea of the global processes occurring upon ΔCC3-TAX1BP1 expression and try to pin-point specific TAX1BP1 interactors that could be indicative of distinct non-classical autophagic processes, mass-spectrometry analysis of TAX1BP1 precipitates was performed. Here, HIS-tagged TAX1BP1 was co-precipitated under native conditions by means of Ni-NTA pulldown and the pulled down fractions were further analyzed by mass-spectrometry. Both conditions of depolarization only (16h CCCP) or depolarization combined with autophagic flux blockage (16h CCCP + BafA) were analyzed.

Identified protein groups and peptides showed a minor increase for cells expressing TAX1BP1 in its WT and mutated forms when compared to the empty plasmid (Figure S7A-B). Furthermore, comparisons of the numbers of protein groups connected to mitochondria as well as the autophagy and vesicular transport machineries revealed no sample specific differences (Figure S7A). The overall sample correlations were high and principal component analysis indicated that the main differences between samples stemmed from variations between replicates (Figure S7C-D). As further quality control of the dataset, the number of identified peptides for TAX1BP1 peptides and protein quantity were investigated. As expected, TAX1BP1 was found to be absent in the control samples (Fig. S7E-F). Surprisingly, K549R-TAX1BP1 quantity values were lower in comparison to WT and ΔCC3 (Fig. S7F). Statistical differences were analyzed between ΔCC3- and WT- TAX1BP1 upon CCCP treatment only (Figure S8A) or in combination with BafA (Figure 8A). Here, when comparing ΔCC3- with WT-TAX1BP1 after extended depolarization only, an increased co-precipitation of inner mitochondrial proteins was identified (Figure S8A). These findings are in line with the identified delayed mitochondrial degradation phenotype of ΔCC3-TAX1BP1 during earlier depolarization (Figure 4B). On the other hand, when comparing ΔCC3- and WT- TAX1BP1 upon CCCP combined with BafA inhibition, multiple proteins involved in vesicle-mediated transport, mitophagy or mitochondria localized proteins were significantly regulated (Figure 8A).

Significantly up- and downregulated proteins were further analyzed for statistical overrepresentation on GO biological processes for the condition of depolarization combined with autophagy flux blockage only, using the panther database (www.pantherdb.org, version 19.0) (Mi *et al.*, 2013). Upon comparing the protein signatures interacting with ΔCC3 against

WT under CCCP and BafA treatment combined, GO-term analysis indicated a downregulation of several vesicle-related biological processes, some of them related to retrograde transport or vesicle budding. Moreover, an upregulation of DNA replication, repair and translation processes and an additional upregulation of mitophagy response processes related to mitochondria depolarization were identified (Figure 8B).

When analyzing the protein signatures interacting with ΔCC3 under these conditions in more detail, a downregulated co-precipitation of TAX1BP1 with several proteins involved in intracellular trafficking was identified (Figure 8A). Those included the Rab-GTPases RAB8A, RAB14 and RAB1A, proteins involved in membrane organization (TMEM33, VPS33A) and other proteins involved in endosome budding from the Golgi apparatus (ARF1, ARF4). On the other hand, an upregulated interaction with ubiquitin and inner mitochondrial proteins was found (Figure 8A). This later finding correlates with previous data showing an increased amount of enlarged ΔCC3-TAX1BP1-positive vesicles carrying increased amounts of mitochondrial material. Additionally, several vesicular-trafficking related proteins were identified to increasingly co-precipitate with ΔCC3-TAX1BP1. Those were: three COPII vesicle-related proteins (SEC31A, SEC24D and SEC24A) (Wang *et al.*, 2017), the endocytosis-related protein epsin-1 (EPN1) (Bhattacharjee *et al.*, 2021), the Rab6-intercting protein ELKS/ERC1 involved in exocytosis (Hida and Ohtsuka, 2010; Ramella, Ribolla and de Curtis, 2022) and the GTPase activating protein ACAP2, known to be involved in endosomal trafficking (Jackson *et al.*, 2000) (Figure 8A). Moreover, at a lower significance level (p-value<0.1), an upregulation of autophagy-related protein WDR45B/WIPI3 as well as the Rab7 GTPase activator TBC1D15 were identified (Figure 8A), both also implicated in mitophagy or general autophagy (Yamano *et al.*, 2014, 2018; Bakula *et al.*, 2017; Ji *et al.*, 2021). Importantly, no significant interaction with ubiquitin or vesicle-related proteins was observed for K549R-TAX1BP1 while an additional interaction with mitochondrial proteins was identified (Figure S8B).

These data indicate that ΔCC3-TAX1BP1 under these conditions is capable of dysregulating vesicle-trafficking processes while is able to increasingly interact with ubiquitinated mitochondrial targets. Overall, these findings reinforce the hypothesis that ablating ubiquitination at CC3 of TAX1BP1 impairs its mitochondrial targeting efficacy which may in turn additionally have an effect at later stages of autophagy, when autophagosomes are formed and vesicular transport is essential for autophagosome maturation.

Discussion

Complete mitochondria elimination during PINK1/Parkin mitophagy is subject to autophagy adaptor-dependent recognition of ubiquitinated mitochondria. In this context, five autophagy adaptors have been linked to PINK1/parkin mitophagy: NBR1, p62/SQSTM, OPTN, NDP52 and TAX1BP1 (Dikic and Elazar, 2018). PTMs are known to play a regulatory role on autophagy adaptor functionality during selective autophagy (Lechado-Terradas *et al.*, 2021). Here we show that TAX1BP1 ubiquitination at its CC3 domain can regulate TAX1BP1-mediated degradation of depolarized mitochondria during PINK1/parkin mitophagy, compromising the efficiency of mitochondrial cargo delivery when TAX1BP1 lacks CC3-ubiquitination.

TAX1BP1 ubiquitination at K549 or other lysines within its CC3 domain have been reported under similar mitochondria depolarizing conditions as the ones reported in this study (Figure 1) (Sarraf *et al.*, 2013; Rose *et al.*, 2016), strongly suggesting a regulatory role for this PTM. Indeed, we could observe that TAX1BP1 ubiquitination did not direct the autophagy adaptor for early proteasomal degradation (Figure S1A) but instead, ubiquitinated TAX1BP1 was found enriched in mitochondria fractions upon short depolarization (Figure 2B). Another fact that strengthens this hypothesis is not only that the CC3 domain is richer in lysins in comparison to the other coiled-coiled regions of TAX1BP1, but that the lysins encoded within the CC3 domain are highly conserved across mammalian species (Figure S3). Indeed, when deleting the CC3 domain of TAX1BP1 a clear decrease in total TAX1BP1 ubiquitination was observed, both after short (4h CCCP) and extended depolarization combined with autophagy flux inhibition (16h CCCP + BafA) (Figure 3B, 5E and S2C). Interestingly, when checking TAX1BP1 predicted structure in AlphaFold (Jumper *et al.*, 2021), the structure of the regions connecting the different CC domains and the UBD with the CC3 are of lowest confidence (Figure S9A). This could be indicative of a highly dynamic behavior of those regions, which could in turn influence the orientation of the distinct CC and UBD regions. Thus, while there is no evidence for a potential structural interaction between the CC3 and UBD regions based on the AlphaFold model, it is tempting to speculate that the ubiquitination of multiple lysines at the CC3 could influence the orientation or availability of the UBD region (Figure S9B).

Abolishing TAX1BP1 ubiquitination at CC3 domain had a negative impact in TAX1BP1 efficiency, promoting a delayed TOM20 degradation (Figure 3B-C) and a slower clustering

of mitochondria after short depolarization (Figure 4A-D). Moreover, while CC3 ubiquitination was proven not essential for TAX1BP1 translocation to mitochondria (Figure 4A), a lack of it did significantly reduce the distribution of the autophagy adaptor on depolarized mitochondria (Figure 4E-F). Thus, indicating that the delayed mitochondrial degradation and clustering of ΔCC3-TAX1BP1 was possibly due to an impairment on depolarized mitochondrial recognition. One of the first reports describing TAX1BP1 domain structure and its first links to immunity-related functions, described three different coiled-coil domains localized between the now known SKITCH and UBA domains (Ling and Goeddel, 2000). Interestingly, Ling and Goeddel identified the CC1 and CC2 domains to be essential for TAX1BP1 homodimerization under basal conditions, while the region flanking the CC3 seemed to play a minor role in its assembly (Ling and Goeddel, 2000). Similarly to TAX1BP1, the autophagy adaptor NDP52 also possesses a central CC region recently identified to be crucial for NDP52 homodimerization in the context of mitophagy (Johansen and Lamark, 2011; Kataura *et al*., 2023). Based on this, is tempting to speculate that the differences observed in ΔCC3-TAX1BP1 distribution on mitochondrial material might be due to a reduced homodimerization capacities. However, it is also possible that due to the localized ΔCC3-TAX1BP1 mitochondrial recognition, autophagosome biogenesis can only occur those localized TAX1BP1 active sites, simply delaying the packaging of damaged mitochondrial material.

Our study also reveals that, even though the lack of ubiquitination at CC3 does not impair complete mitochondrial degradation, the degradative pathways governing this process may differ between WT and ΔCC3, as an increased presence of enlarged degradation vesicles was observed in ΔCC3 (Figure 5A-D). It is noteworthy that these enlarged vesicles were prominently surrounded by the PD gene product VPS35, suggesting a functional link between the mitophagy pathway regulated by the most common recessive gene products PINK1 and parkin, and the rare VPS35 gene product that is suggested to be involved in vesicle trafficking effects of the common dominant PD gene product LRRK2. Yet, we could not identify a unique endolysosomal marker specific for the enlarged degradative vesicles only, as all enlarged and small vesicles were positive for LC3B, VPS35, RAB7 and CD63 (Figure 6 and S5). Nevertheless, important structural differences were observed between small and enlarged vesicles. The enlarged ΔCC3-TAX1BP1-positive structures contained numerous TAX1BP1/LC3B-positive vesicles carrying mitochondrial material and where globally surrounded by RAB7/VPS35/CD63-positive vesicles (Figure 6). On the other hand,

small vesicles found in all TAX1BP1 constructs consisted of single TAX1BP1/LC3B-positive vesicles also carrying mitochondrial material and positive for the endolysosomal markers RAB7, CD63 and VPS35 (Figure S6). These data seem to indicate that the degradation pathways involved in WT and ubiquitination deprived TAX1BP1 are possibly of the same nature and the identified enlarged and small vesicles are the result of autophagosomes fusion with endosomes (amphisomes) or lysosomes (autolysosomes) (Zhao, Codogno and Zhang, 2021). Autophagosome fusion with endosomes is known to be necessary for autophagosome maturation as it increases the pH of the degradative vesicle and is considered a previous step for lysosome fusion (Zhao, Codogno and Zhang, 2021). On the other hand, autophagy flux inhibition via BafA does not specifically hinder the fusion of autophagosomes with lysosomes (Mauthe *et al.*, 2018), thus we cannot discard that the observed enlarged TAX1BP1-positive vesicles could be autolysosomes. TAX1BP1 has been reported to interact with the cytoskeletal motor myosin VI (MYO6), known to be involved in endocytic transport and to facilitate autophagosome maturation by interacting with the UBD of TAX1BP1 (Tumbarello *et al.*, 2012). Interestingly, compromising autophagosome maturation via transient knock-down of MYO6, induced the formation of immature enlarged autophagosomes positive for p62/SQSTM (Tumbarello *et al.*, 2012). Another recent example of the relationship between degradative vesicle size and endosome/autopagosome maturation was achieved by transient knockdown of individual HOPS complex subunits, known to play an essential role in endosome and autophagosome fusion with lysosomes (der Beek *et al.*, 2024). Based on this, it seems reasonable to think that the enlarged vesicles observed in ΔCC3-TAX1BP1 are the result of impaired autophagosome maturation driven by ΔCC3-TAX1BP1 alone and further accentuated by BafA treatment.

The formation of enlarged degradative vesicles was not only observed in 5KO HeLa (Figure 5D and Figure 6) but also in parental HeLa with all complementary autophagy adaptors (Figure 7A). In this case, the observed ΔCC3-TAX1BP1-positive structures were generally smaller as the ones observed in 5KO HeLa. However, amongst the regularly sized TAX1BP1-positive structures, an increased proportion of enlarged ΔCC3-TAX1BP1-positive structures were observed (Figure 7C-D). These data indicate that while the presence of complementary autophagy adaptors can partially compensate for the observed phenotype, the ΔCC3-dependent formation of enlarged degradative vesicles can be considered of a dominant nature. Moreover, the mitochondrial material recognized by the TAX1BP1-positive

enlarged vesicles was significantly increased in ΔCC3 and K549R in comparison to WT (Figure 7G), strongly suggesting a decreased efficiency of ΔCC3, also under conditions of complementary autophagy adaptor expression. As the largest TAX1BP1 vesicles were only observed in 5KO HeLa, the expression of complementary autophagy adaptors can partially compensate for the TAX1BP1-dependent formation of enlarged degradative vesicles. This is in agreement with previous reports indicating TAX1BP1 as the least efficient autophagy adaptor to promote PINK1/parkin mitophagy in 5KO HeLa (Lazarou *et al.*, 2015). In addition, recent reports using proximity-labelling approaches have indicated that TAX1BP1 can interact with other autophagy adaptors during mitophagy (Heo *et al.*, 2019; Zellner, Schifferer and Behrends, 2021) suggesting the cooperation with more efficient autophagy adaptors can partially compensate for ΔCC3-TAX1BP1 compromised efficiency.

Upon general GO-Term analysis of ΔCC3-TAX1BP1 native pulldown (Figure 8B), a significant decrease in interactions related to general vesicle trafficking was identified and is in agreement with previous results showing an increased presence of ΔCC3-TAX1BP1-positive enlarged vesicles under these conditions (Figure 5D and 6). An upregulated interaction with inner mitochondrial proteins and ubiquitin confirmed a decreased efficiency of ΔCC3 in mitochondria degradation (Figure 3C, 4B-D and 8A). However, expected TAX1BP1 interactors like FIP200 or MYO6 could not be detected for neither of the mutants or WT-TAX1BP1. The increased interaction of ΔCC3-TAX1BP1 with ubiquitin and the lack of MYO6 co-precipitation may be indicative of delayed ubiquitinated mitochondria recognition, as MYO6 binding competes with ubiquitin at the UBD of TAX1BP1 (Tumbarello *et al.*, 2012).

On the other hand, an upregulated interaction of ΔCC3-TAX1BP1 with the components of COPII vesicle coat complex SEC24A, SEC24D, SEC31A and the receptor-mediated endocytosis EPN1 were identified (Morinaka *et al.*, 1999; Stankewich, Stabach and Morrow, 2006; Mancias and Goldberg, 2008) (Figure 8A). Similarly, albeit at a lower-significance level, an increased interaction of two autophagy-related proteins involved in autophagosome biogenesis (WDR45B and TBC1D15) was observed (Figure 8A). Importantly, COPII vesicles are known to be important source of membrane lipids for the formation of autophagosomes and indeed, recent reports have demonstrated that both SEC24 and SEC31 can interact with ATG9 vesicles, directly influencing autophagosome biogenesis (Davis *et al.*, 2016; Hurley and Young, 2017; Nie *et al.*, 2024). Similarly, the Rab GTPase activating protein

TBC1D15 is closely implicated with mitophagy progression via its capacity to modulate active RAB7 levels at the OMM and favor autophagosome biogenesis (Yamano *et al.*, 2014, 2018). On the other hand, WDR45B (WIPI3) is known to localize at nascent autophagosomes as well as in late endosomes and thus seems to also play a role in autophagosomes biogenesis and maturation (Bakula *et al.*, 2017; Ji *et al.*, 2021). Thus, given that ΔCC3-TAX1BP1 expression induced a delayed degradation of mitochondrial material, it seems reasonable to think that the interaction of ΔCC3-TAX1BP1 with the autophagosome biogenesis-related proteins at such later stage of the pathway is probably due to a slower capability of the autophagy adaptor to recruit these and other autophagy-related proteins in charge of autophagosome biogenesis. On the other hand, decreased interactions were observed for the Rab GTPases RAB14, RAB1A and RAB8A, the ER-transmembrane protein TMEM33 and the HOPS complex member VPS33 (Figure 8A). Rab GTPases are generally involved in endosomal vesicle trafficking but have also been described to play a role in modulating autophagy. RAB1A has been described to be essential for autophagosome formation (Gyurkovska *et al.*, 2023; Haga and Fukuda, 2024) while RAB14 is implicated in autophagosome maturation (Haga and Fukuda, 2024). Similarly, VPS33A acts as a tether between autophagosomes and lysosomes to facilitate their fusion (Wartosch *et al.*, 2015; Zhao, Codogno and Zhang, 2021). Potential defects in autophagosome maturation would be in agreement with the identified sustained ubiquitin interaction, considering that MYO6 interaction competes with ubiquitin at the UBD of TAX1BP1. Overall, our data suggest that the vesicle-trafficking defects identified in ΔCC3-TAX1BP1 may be due to impaired autophagosome biogenesis or maturation.

Conclusions

In this study, we identified the CC3 of TAX1BP1 as a highly ubiquitinated region during PINK1/parkin mitophagy which is not essential for complete mitochondria degradation. However, lack of CC3 ubiquitination delayed mitophagy progression, reduced TAX1BP1 distribution on mitochondrial material and impaired vesicular trafficking. The identified vesicular trafficking defects may be driven by a delayed initiation of autophagosome biogenesis as well as an impairment with autophagosome maturation and are a reflection of the identified lower degradative efficiency of ΔCC3-TAX1BP1 via an alternative mitophagy pathway.

Materials and methods

Cell culture, treatments and transfections

All cell lines were grown at 37°C and 5% CO_2 with high-glucose Dulbecco's modified eagle medium (DMEM). WT-Parkin and 5KO-PRKN HeLa were supplemented with 0.7 mg/ml geneticin to ensure stable parkin expression. HeLa cells stably expressing WT or inactive mutant (C431A) were previously described (Geisler *et al.*, 2019). To obtain 5KO HeLa stably expressing WT-Parkin (5KO-PRKN HeLa), cells were transfected with BglII linearized pcDNA3.1-3xFlag-Parkin for 24 hours and were further selected with 1.8 mg/ml of Geneticin (Merk Millipore) for 13 days. Upon selection, clones were screened for homogenous Parkin expression. Mitophagy induction was achieved with 10 µM CCCP (Sigma) for the indicated time-points. Proteasome and autophagy inhibition were induced with 10 µM MG132 (Sigma) or 400 nM BafA (Chemcruz), respectively. Inhibition treatments were initiated half an hour before CCCP treatment and were maintained in combination with CCCP for the indicated periods. Long CCCP treatment of 5KO-PRKN HeLa was combined with 60 µM Q-VD-Oph (QVD, Selleckchem #S7311) to prevent cell death. Transient transfection of the indicated constructs was performed with FuGENE6® (Promega), following manufacturer's instructions. HeLa cells were transfected with 5 nM of siRNA for three consecutive days using Hiperfect (Qiagen). The following siRNA were used: negative control (AllStars negative, SI03650318); TAX1BP1_7, 5'-CAGATCAATCAGCTAATAATA-3' (SI02781268); TAX1BP1_9, 5'-AAGGGTCTTACTGAAGTAACA-3' (SI03036124); TAX1BP1_8, 5'-CAGTCTTTGGCTTATCAATAA-3' (SI02781296).

Expression constructs

The construct pcDNA3.1-3xFlag-Parkin has been described previously (Geisler *et al.*, 2014) and was used to transiently express parkin in 5KO HeLa and to generate the stable 5KO-PRKN as previously explained. Full length WT-, K549R- and ΔCC3-TAX1BP1 cDNA were amplified from commercial vectors obtained from Origene (WT TAX1BP1, Cat Num: RC208233) or eZyvec on demand (K549R and ΔCC3, Quote: D2022-10) and were sub-cloned into pCMV-6HIS vector to ensure equal expression conditions. Obtained constructs were further sequenced prior to use.

Western blotting

Upon treatment, cells were washed once with phosphate-buffered saline (PBS) and directly harvested. For whole cell lysate samples, cell pellets were resuspended in urea lysis buffer (10 mM Tris, pH 8.0, 100 mM NaH_2PO_4, and 8 M urea) after a short centrifugation step (972 x g for 1 min at 4°C). Lysates were passed through a 26-gauge needle to break the DNA for at least 5 times. Whole cell lysate fractions were obtained after pelleting debris at 3151 x g for 15 min at 4°C. Protein concentration was measured using the Bradford Protein Assay Kit (Bio-Rad) following manufacturer's instructions. Proteins were separated using 4-12%, 3-8% pre-casted (Invitrogen) or self-casted polyacrylamide gels and were run at a fixed voltage of 80-100V for at least 1,5 hours at room temperature (RT). Proteins were transferred to polyvinylidene fluoride (PVDF) membranes (Immobilon-P, Merck) at constant voltage of 25V or 100V for an overnight run or 2 hours, respectively. Upon transfer, membranes were blocked with 5% non-fat dried milk in Tris-buffered saline containing 0.1% Tween-20 (TBS-T). Membranes were incubated with primary antibodies for 2h at RT or overnight at 4ºC. After three consecutive TBT-T washes of 5 minutes, membranes were incubated with the corresponding secondary antibodies diluted in 5% of non-fat dried milk for 1 hour at RT. Upon additional three TBT-T washes of 5 minutes, protein bands were visualized using chemiluminescent-horseradish peroxidase (HRP) substrate (Merk-Millipore) and Ultracruz autoradiography films (Santa Cruz Biotechnology).

Immunofluorescence

HeLa cells were seeded in PDL pre-coated coverslips. After treatment, cells were fixed with 4% PFA for 20 minutes. After fixation and three consecutive washes with PBS, permeabilization was performed with 1% Triton-X for 5 minutes at room temperature (RT). After three washing steps with PBS, blocking was performed at RT for 1 h with 10% fetal bovine serum or donkey serum (blocking buffer). Afterwards, coverslips were incubated with the corresponding primary antibodies diluted in blocking buffer for 2 h at RT. After three washing steps with PBS, coverslips were incubated with secondary antibodies diluted in blocking buffer for 1 h at RT. Following three additional washing steps with PBS, nuclei were stained with 2 µg/ml of Hoechst 33342 in PBS for 5 minutes at RT. After incubation, three additional washing steps with PBS were performed. Coverslips were finally mounted with fluorescent mounting media (Dako, Agligent). Imaging was performed using an AxioImager microscope equipped with Apotome imaging system (Carl Zeiss). Images were processed

with the ZEN 2.3 lite software and Image J. For LC3B immunostaining, cells were fixed with ice-cold methanol for 2-3 minutes. Further immunostaining steps were performed as previously described. Image acquisition of endogenous LC3B was realized with a Nikon Ti2e spinning disk confocal microscope. In this case, images were processed using the NIS-Elements software (Nikon).

Eye-based quantification of TAX1BP1 colocalization on COX4 (Figure 4F) was performed by taking into account only TAX1BP1-positive cells with COX4 clumps after 4h CCCP treatment, to account for parkin-positive cells. TAX1BP1 behavior was classified between complete or localized apposition of COX4 clump depending on its distribution. In situations where both TAX1BP1 behaviors were observed in the same TAX1BP1-positive cell, localized apposition of TAX1BP1 with COX4 cluster was considered. Quantification of complete mitochondria elimination upon TAX1BP1 transfection (Figure 5C) was achieved by only taking into account parkin-positive cells only (empty control) or cells positive for both parkin and TAX1BP1 (TAX1BP1 transfection) after CCCP treatment. Cells were considered to be cleared of mitochondria where no SSBP1 puncta were observed. Quantification of small or enlarged TAX1BP1-positive structures was performed by taking into account only parkin-positive cells. Cells were classified between containing small or enlarged TAX1BP1 structures according size. In situations where both enlarged and small TAX1BP1 structures were observed in the same TAX1BP1-positive cell, the cell was quantified as containing enlarged TAX1BP1 structures.

Antibodies

Antibody	WB	IF	Provider	Catalog number
Actin	1:50000, 1:10000	-	Sigma Aldrich, Merk	A5441
Calnexin	1:10000	-	Enzo Life Sciences	ADI-SPA-860
CD63	-	1:250	Antibodies online	ABIN94214
COX4	-	1:10000	Cell signaling	4850
CS	1:6000	-	GeneTex	GTX110624
Flag	1:10000	-	Sigma-Aldrich	F1804
HIS	-	1:500	Addgene	184180
HSP60	-	1:10000	Novus Biologicals	NBP3-05536
LAMP1	1:10000	1:500	DSHB Hybridoma bank	Clone H4A3
LC3B	1:10000	-	GeneTex	GT3612

LC3B	1:10000	1:500	Cell signaling	835065
MFN1	1:10000	-	Abnova	H00055669-M04
NBR1	1:10000	-	ProteinTech	16004-1-AP
NDP52	1:10000	-	ProteinTech	12229-1-AP
OPTN	1:10000	-	Atlas antibodies	HPA003360
p62/SQSTM	1:10000	-	BD Biosciences	#610832
Parkin	1:50000	1:10000	Cell signaling	4211S
RAB7	-	1:200	Cell signaling	95746
TAX1BP1	1:1000; 1:10000	1:500	Novus Biologicals	NBP1-86662
TOM20	1:30000	-	Santa Cruz	sc-17764
TOM20	1:6000	-	Proteintech	11802-1-AP
VDAC	1:10000	-	ProteinTech	66345-1
VDAC	1:30000	-	Millipore	AB10527
Vinculin	1:50000, 1:10000	-	Sigma Aldrich	V9131
VPS35	-	1:250	Novus Biologicals	NB100-1397
Anti-mouse HRP	1:10000	-	Amersham Pharmacia	115-035-003
Anti-rabbit HRP	1:10000	-	Amersham Pharmacia	111-035-003
Donkey anti-sheep Alexa Fluor 647	-	1:1000	Invitrogen	A-21448
Donkey anti-mouse Alexa Fluor 488	-	1:1000	Invitrogen	A-21202
Donkey anti-mouse Alexa Fluor 568	-	1:1000	Invitrogen	A-10037
Donkey anti-rabbit Alexa Fluor 488	-	1:1000, 1:500	Invitrogen	A-21206
Donkey anti-rabbit Alexa Fluor 568	-	1:1000	Invitrogen	A-10042
Donkey anti-chicken Alexa Fluor 647	-	1:1000	Invitrogen	A78952
Donkey anti-goat Alexa Fluor 648	-	1:1000	Invitrogen	A21447
Donkey anti-goat Alexa Fluor 488	-	1:1000	Invitrogen	A11055

693 Mitochondria fractionation

694 Mitochondria purification was performed as described in (Alberio *et al.*, 2017) with some
695 modifications. Cell pellets were first resuspended in mitochondrial buffer (MB) (210 mM
696 mannitol, 70 mM sucrose, 10 mM HEPES, 1 mM EDTA at pH 7.5) and further cell lysis was
697 performed mechanically using a glass homogenizer. After a first lysing series of 30
698 mechanical stokes, cell homogenates were centrifuged at 600 x g for 10 min 4ºC. The

remaining pellet was resuspended with the remaining supernatant and two additional lysing series were performed, with an in-between centrifugation step (600 x g for 10 min 4ºC). After the first and last centrifugation the remaining supernatant was recovered (corresponds to F1). The remaining pellet was resuspended in 800 µl MB and was centrifuged at 700 x g for 10 min at 4ºC to obtain the crude mitochondria pellet and the second supernatant fraction (F2). Crude mitochondria pellets were resuspended in 250 µl MB and layered into a discontinuous sucrose gradient formed by a 6 ml layer of 1.2 M sucrose over a 5 ml layer of 1.6 M sucrose using ultra-clear tubes (14 x 89mm, Beckmann). Loaded gradients were centrifuged using a Beckman ultracentrifuged equipped with a SW40Ti rotor at 96000 x g for 2 hours at 4ºC (acceleration and deceleration parameters were set to 3). Upon centrifugation, bands of interest were recovered. On the lighter sucrose layer, the band corresponding to membrane fraction (MMF) was collected and at the layer interface, the band corresponding to enriched mitochondria fraction (MTF) was collected. Upon collection, sucrose was diluted with four volumes of MB and all fractions were pelleted at 13000 x g for 10 min at 4ºC. Pellets were resuspended in urea buffer (10 mM Tris, pH 8.0, 100 mM NaH2PO4, and 8 M urea). Equal protein amounts of each fraction were subjected to Western blot analysis.

Native Ni-NTA pulldown

Cells were pelleted at 1000xg for 1 min at 4°C. Pellets were lysed with native lysis buffer (50 mM NaH_2PO_4, 300 mM NaCl, 0.2% NP-40, pH 8.0) complemented with 25 mM Imidazole, protease and phosphatase inhibitors (Roche). Lysed pellets were incubated on ice for 30 minutes. After incubation, lysed pellets were centrifuged at 12000xg for 15 minutes at 4°C and supernatant was collected for total protein quantification. Ni-NTA spin columns (Qiagen) were used to purify 6HIS-tagged TAX1BP1 and its interacting proteins following provider instructions. Briefly, Ni-NTA spin columns were first equilibrated using native lysis buffer with 25 mM Imidazole and centrifuged for 2 minutes at 890xg. After equilibration, 250 µg of total protein was loaded on the columns and lysates were centrifuged at 270xg for 10 minutes. Ni-NTA columns were washed three times with lysis buffer containing 50 mM imidazole, centrifuged for 2 minutes at 890xg. After washing, pulldown fractions were collected with elution buffer (50 mM NaH_2PO_4, 300 mM NaCl, 0.2% NP-40, 500 mM Imidazole, pH 8.0) at 890xg for 2 minutes twice. Samples were sent directly in elution buffer for mass spectrometry analysis.

Mass spectrometry

Eluates were mixed with of 4x LDS sample buffer and proteins were separated by short SDS-PAGE runs using NuPAGE NovexR Bis-Tris 4 – 12 % Mini Gels (Invitrogen). Protein bands were stained using QC Colloidal Coomassie Stain (Bio-Rad Laboratories) and whole sample lanes were excised. Gel pieces were further cut into small pieces prior to in-gel digestion. Gel pieces were destained by incubation with 5 mM ABC in 50 % (v/v) ACN for 20 minutes three times and dehydrated using acetonitrile. Cysteine bonds were reduced by incubation with 10 mM DTT for 45 minutes at 65 °C before carbamidomethylation by incubation with 55 mM iodoacetamide for 45 minutes at RT in the dark. Gel pieces were washed two times and dehydrated as before, followed by digestion with trypsin overnight at 37 °C. Peptides were extracted in three consecutive incubation steps with Extraction buffer A (50 % (v/v) ACN, 3 % trifluoroacetic acid (TFA)), Extraction buffer B (80 % (v/v) ACN, 0.5 % (v/v) Trifluoroacetic acid (TFA)) and acetonitrile for 30 minutes each. Supernatants of each extraction were pooled, and acetonitrile was evaporated by vacuum centrifugation. Peptides were purified using StageTips (Rappsilber, Mann and Ishihama, 2007). Mass spectrometric analysis was performed using an Orbitrap Exploris 480 online coupled to an EASY nLC-1200 system (Thermo Fisher Scientific). Peptides were separated on a 20 cm HPLC column with 75 µm inner diameter (CoAnnTech) in-house packed with 1.9 µm ReproSil-Pur C18 -AQ silica beads (Dr Maisch GmbH) and eluted by solvent B in a 60-minute linear gradient from 5 – 33 % at a flow rate of 200 nL/min. Carry-over was minimized by 30-minute wash runs after each sample. Ionization was performed by ESI and the mass spectrometer was operated in positive ion mode controlled by XCalibur (Thermo Fisher Scientific).

Acquisition of spectra was performed with a scan range of 350 – 950 m/z and a resolution on the MS1 level of 60 000. MS2 scans were performed using DIA isolation windows of 8 m/z with an overlap of 1 m/z (75 isolation windows), HCD collision energy of 30 % and resolution of 15 000.

Mass spectrometry analysis

Raw files were processed using Spectronaut version 19 in directDIA+ mode using optimized identification settings as described before (Bruderer *et al.*, 2017). Spectra were predicted using a Uniprot *Homo sapiens* database (104 556 entries, downloaded on 2024/01/30). The data were exported using the protein pivot report using PG.ProteinGroups as a unique

protein id and the PG.Quantity as a quantification column. Data analysis was performed using Perseus version 2.0.5.0 (Tyanova *et al.*, 2016) and Microsoft Excel and R. Proteins were annotated functionally and by compartment using Gene Ontology Biological Processes and Gene Ontology Cellular Compartment databases (both downloaded on 2024/10/29) as well as for mitochondrial sub-compartments using MitoCarta3.0 (downloaded on 2021/02/24). To assess differences between WT- and mutant TAX1BP1, student's T-tests were performed on protein intensities normalized to the protein quantities of the empty vector for both CCCP only and CCCP and BafA treated samples. Significantly up- and downregulated proteins ($p<0.05$) were further analyzed for statistical overrepresentation on GO biological processes using the panther database (pantherdb.org, version 19.0) (Mi *et al.*, 2013).

CellProfiler-based image analysis

The version 4.2.1 of the CellProfiler software was used (Stirling *et al.*, 2021). All analyses rely on pooled single cell values obtained from at least three independent biological replicates. In general, individual cells were initially recognized with the nuclear staining and a cytoplasm area of 80-200 pixels (px) around the nucleus was further categorized as the cytoplasm, unless otherwise noted. Areas of interest per cell correspond to the established cytoplasm without the nucleus area.

For the analysis of mitochondrial clustering in WT-Parkin HeLa transfected with His-empty or HIS-wtTAX1BP1, mitochondrial material was recognized using SSBP1 signal as primary object. SSBP1 objects were identified using a two-class thresholding Robust background method with a lower and upper threshold bounds of 0.0-1.0, an adaptive window of 50 and a size range of 6-500 px. Next, single SSBP1 objects that were in close contact were merged (distance between objects= 0px). To account for only positively TAX1BP1 transfected cells, TAX1BP1 was recognized as primary objects using a two-class thresholding Minimum cross entropy method with a lower and upper threshold bounds of 0.0-1.0, an adaptive window of size 30 and a size range of 10-40 px. Only cells with positive TAX1BP1 signal (count TAX1BP1 objects > 0) were taken into account for the TAX1BP1 overexpressing (OE) condition.

For the analysis of mitochondria clustering in 5KO HeLa co-expressing parkin as well as WT-, K549R and ΔCC3-TAX1BP1, the analysis was performed similarly as previously

794 described for the WT-Parkin HeLa with some variations. Mitochondrial material was
795 recognized as SSBP1 signal using a two-class thresholding Roust backgroung method with
796 a lower and upper threshold bounds of 0.002-1.0, an adaptive window of size 50 and a size
797 range of 4-500 px. TAX1BP1 was recognized as primary objects using a two-class
798 thresholding Minimum cross-entropy method with a lower and upper threshold bounds of
799 0.0022-1.0, an adaptive window of size 80 and a size range of 6-40 px. Similarly, Parkin
800 expression was monitored by recognizing parkin signal as primary object using two-class
801 thresholding Minimum cross-entropy method with a lower and upper threshold bounds of
802 0.0015-1.0, an adaptive window of size 50 and a size range of 10-40 px. Parkin objects were
803 further merged if they were in close contact (distance = 0 px). Only cells with positive
804 TAX1BP1 and parkin signal (mean object area > 0) were taken into account for this analysis.
805 Values of total mean SSBP1 area and mitochondrial area or perimeter normalized by cell
806 size (area or perimeter) are shown. For the analysis of TAX1BP1 distribution on SSBP1
807 clusters, only cells with a mean TAX1BP1 intensity of ≥10 aiu (arbitrary intensity units) were
808 taken into account and the recognition method of TAX1BP1 and parkin signals was
809 optimized. In this case, TAX1BP1 and parkin were recognized as primary objects using a
810 two-class thresholding Robust background method with lower and upper threshold bounds
811 of 0.0035-1.0 (TAX1BP1) or 0.002-1.0 (parkin) with a size range recognition of 3-40 px in
812 both cases. Mitochondria were recognized using SSBP1 signal as described before for 5KO
813 HeLa. To measure the overlapping area between TAX1BP1-SSBP1 and parkin-SSBP1,
814 total SSBP1 area was masked with TAX1BP1 or parkin merged objects and the percentage
815 of SSBP1 overlapped by each protein was calculated (% SSBP1 recognized). Similarly,
816 percentages of TAX1BP1 or parkin on mitochondria were calculated by considering which
817 portion of the total TAX1BP1 or parkin area was engaged with mitochondrial material (%
818 TAX1BP1/parkin on SSBP1).

819 For the analysis of size classification of TAX1BP1-positive puncta and TAX1BP1-HSP60
820 material overlap in WT-Parkin HeLa, cell area was recognized using a Watershed-image
821 method with nuclei as a reference point and TAX1BP1 signal to identify cell contours
822 (Minimum cross entropy method, threshold bounds: 0.00001-1). TAX1BP1 puncta were
823 recognized as primary objects using Robust background method with lower and upper
824 threshold bounds of 0.000001-1.0, an adaptive window of size 15 and a size range of 4-40
825 px. In the conditions of OE TAX1BP1, only cells with TAX1BP1 mean intensity of 0.004 aiu
826 were considered. To optimize the recognition of individual puncta, clumped objects were

distinguished by shape but dividing lines between clumped objects were intensity-based. TAX1BP1 objects were merged when in contact with each other (distance = 0 px), this step allowed to merge TAX1BP1 puncta that were in close contact with multiple other TAX1BP1 puncta and were particularly difficult to recognize as single objects. Upon merging TAX1BP1 single objects, objects with an area form factor of 0.68-0.8 were kept (form factor=1 for a perfectly circular object). This step allowed to keep relatively circular-shaped objects and discard merged objects that were the result of multiple TAX1BP1 puncta. Thus, not all TAX1BP1 puncta were taken into account for this analysis. After filtering, TAX1BP1 puncta were classified based on their size: enlarged puncta (area>150 px^2), intermediate puncta (area≤150 px^2) and small puncta (area<50 px^2). Mitochondrial material (HSP60) was recognized as primary object using a Robust background method with lower and upper threshold bounds of 0.001-1 and a size range of 1-40 px. HSP60 objects were used to mask enlarged, intermediate and small TAX1BP1 puncta. All TAX1BP1 puncta sizes were classified between HSP60-positive or HSP60-negative according to their overlap. Percentages of HSP60 puncta co-localizing with overall or enlarged TAX1BP1 puncta are shown as well as the corresponding HSP60 puncta area co-localizing with enlarged TAX1BP1 puncta. For each analyzed image of this analysis, output images were generated, showing the localization of the classified TAX1BP1 puncta, the cell limits.

Statistics

All data is derived from at least three independent biological replicates unless otherwise indicated. Statistical analysis and graph depiction of the data was performed using GraphPad Prism 8.0.2. Statistical significance was established at $p<0.05$ unless otherwise indicated. Significance was assessed by using a one-way ANOVA for multiple comparisons and subsequent Tukey's post-hoc test. For the correlation analysis of TAX1BP1 binding to depolarized mitochondria, a Pearson correlation test was performed. For analysis in which only two conditions were compared, significance was assessed with an unpaired t-test analysis. The following significance indicators were used: ****: $p<0.001$, ***: $p<0.005$, **: $p<0.005$, *: $p<0.05$

References

Alberio, T. *et al.* (2017) 'Toward the Standardization of Mitochondrial Proteomics: The Italian Mitochondrial Human Proteome Project Initiative', *Journal of Proteome Research*, 16(12), pp. 4319–4329. doi: 10.1021/acs.jproteome.7b00350.

Bakula, D. *et al.* (2017) 'WIPI3 and WIPI4 β-propellers are scaffolds for LKB1-AMPK-TSC signalling circuits in the control of autophagy', *Nature Communications*, 8(May). doi: 10.1038/ncomms15637.

der Beek, J. van *et al.* (2024) 'Loss of the HOPS complex disrupts early-to-late endosome transition, impairs endosomal recycling and induces accumulation of amphisomes', *Molecular Biology of the Cell*, 35(3), pp. 1–24. doi: 10.1091/MBC.E23-08-0328.

Bhattacharjee, S. *et al.* (2021) 'Epsins in vascular development, function and disease', *Cellular and Molecular Life Sciences*. Springer International Publishing, 78(3), pp. 833–842. doi: 10.1007/s00018-020-03642-4.

Bruderer, R. *et al.* (2017) 'Optimization of experimental parameters in data-independent mass spectrometry significantly increases depth and reproducibility of results', *Molecular and Cellular Proteomics*. Â© 2017 ASBMB. Currently published by Elsevier Inc; originally published by American Society for Biochemistry and Molecular Biology., 16(12), pp. 2296–2309. doi: 10.1074/mcp.RA117.000314.

Davis, S. *et al.* (2016) 'Sec24 phosphorylation regulates autophagosome abundance during nutrient deprivation', *eLife*, 5(NOVEMBER2016), pp. 1–22. doi: 10.7554/eLife.21167.

Dikic, I. and Elazar, Z. (2018) 'Mechanism and medical implications of mammalian autophagy', *Nature Reviews Molecular Cell Biology*. Springer US, 19(6), pp. 349–364. doi: 10.1038/s41580-018-0003-4.

Geisler, S. *et al.* (2010) 'PINK1/Parkin-mediated mitophagy is dependent on VDAC1 and p62/SQSTM1', *Nature Cell Biology*. Nature Publishing Group, 12(2), pp. 119–131. doi: 10.1038/ncb2012.

Geisler, S. *et al.* (2014) 'The ubiquitin-conjugating enzymes UBE2N, UBE2L3 and UBE2D2/3 are essential for Parkin-dependent mitophagy', *Journal of Cell Science*, 127(15), pp. 3280–3293. doi: 10.1242/jcs.146035.

Geisler, S. *et al.* (2019) 'Ubiquitin-specific protease USP36 knockdown impairs Parkin-dependent mitophagy via downregulation of Beclin-1-associated autophagy-related ATG14L', *Experimental Cell Research*. Elsevier Inc., 384(2), p. 111641. doi: 10.1016/j.yexcr.2019.111641.

Gyurkovska, V. *et al.* (2023) 'Dual function of Rab1A in secretion and autophagy:

hypervariable domain dependence', *Life Science Alliance*, 6(5), pp. 1–16. doi: 10.26508/lsa.202201810.

Haga, K. and Fukuda, M. (2024) 'Comprehensive knockout analysis of the RAB family small GTPases reveals an overlapping role of RAB2 and RAB14 in autophagosome maturation', *Autophagy*. Taylor & Francis, 21(1), pp. 21–36. doi: 10.1080/15548627.2024.2374699.

Heo, J. M. *et al.* (2015) 'The PINK1-PARKIN Mitochondrial Ubiquitylation Pathway Drives a Program of OPTN/NDP52 Recruitment and TBK1 Activation to Promote Mitophagy', *Molecular Cell*. Elsevier Inc., 60(1), pp. 7–20. doi: 10.1016/j.molcel.2015.08.016.

Heo, J. M. *et al.* (2019) 'Integrated proteogenetic analysis reveals the landscape of a mitochondrial-autophagosome synapse during PARK2-dependent mitophagy', *Science Advances*, 5(11). doi: 10.1126/sciadv.aay4624.

Hida, Y. and Ohtsuka, T. (2010) 'CAST and ELKS proteins: Structural and functional determinants of the presynaptic active zone', *Journal of Biochemistry*, 148(2), pp. 131–137. doi: 10.1093/jb/mvq065.

Hurley, J. H. and Young, L. N. (2017) 'Mechanisms of autophagy initiation', *Annual Review of Biochemistry*, 86, pp. 225–244. doi: 10.1146/annurev-biochem-061516-044820.

Jackson, T. R. *et al.* (2000) 'ACAPs are arf6 GTPase-activating proteins that function in the cell periphery.', *The Journal of cell biology*. United States, 151(3), pp. 627–638. doi: 10.1083/jcb.151.3.627.

Ji, C. *et al.* (2021) 'β-propeller proteins WDR45 and WDR45B regulate autophagosome maturation into autolysosomes in neural cells', *Current Biology*. Elsevier Ltd., 31(8), pp. 1666-1677.e6. doi: 10.1016/j.cub.2021.01.081.

Johansen, T. and Lamark, T. (2011) 'Selective autophagy mediated by autophagic adapter proteins', *Autophagy*, 7(3), pp. 279–296. doi: 10.4161/auto.7.3.14487.

Jumper, J. *et al.* (2021) 'Highly accurate protein structure prediction with AlphaFold', *Nature*. Springer US, 596(7873), pp. 583–589. doi: 10.1038/s41586-021-03819-2.

Kataura, T. *et al.* (2023) 'NDP52 acts as a redox sensor in PINK1/Parkin-mediated mitophagy', *The EMBO Journal*, 42(5), pp. 1–16. doi: 10.15252/embj.2022111372.

Katoh, K., Rozewicki, J. and Yamada, K. D. (2018) 'MAFFT online service: Multiple sequence alignment, interactive sequence choice and visualization', *Briefings in*

Bioinformatics, 20(4), pp. 1160–1166. doi: 10.1093/bib/bbx108.

Kondapalli, C. *et al.* (2012) 'PINK1 is activated by mitochondrial membrane potential depolarization and stimulates Parkin E3 ligase activity by phosphorylating Serine 65', *Open Biology*, 2(MAY). doi: 10.1098/rsob.120080.

Koyano, F. *et al.* (2014) 'Ubiquitin is phosphorylated by PINK1 to activate parkin', *Nature*. Nature Publishing Group, 510(7503), pp. 162–166. doi: 10.1038/nature13392.

Lazarou, M. *et al.* (2015) 'The ubiquitin kinase PINK1 recruits autophagy receptors to induce mitophagy', *Nature*, 524(7565), pp. 309–314. doi: 10.1038/nature14893.

Lechado-Terradas, A. *et al.* (2021) 'Regulation of mitochondrial cargo-selective autophagy by posttranslational modifications', *Journal of Biological Chemistry*. Elsevier B.V, 297(5), p. 101339. doi: 10.1016/j.jbc.2021.101339.

Lechado-Terradas, A. *et al.* (2022) 'Parkin-dependent mitophagy occurs via proteasome-dependent steps sequentially targeting separate mitochondrial sub-compartments for autophagy', *Autophagy Reports*, 1(1), pp. 576–602. doi: 10.1080/27694127.2022.2143214.

Ling, L. and Goeddel, D. V (2000) 'T6BP , a TRAF6-interacting protein involved in IL-1 signaling', pp. 2–7.

Mancias, J. D. and Goldberg, J. (2008) 'Structural basis of cargo membrane protein discrimination by the human COPII coat machinery', *EMBO Journal*, 27(21), pp. 2918–2928. doi: 10.1038/emboj.2008.208.

Matsuda, N. *et al.* (2010) 'PINK1 stabilized by mitochondrial depolarization recruits Parkin to damaged mitochondria and activates latent Parkin for mitophagy', *Journal of Cell Biology*, 189(2), pp. 211–221. doi: 10.1083/jcb.200910140.

Mauthe, M. *et al.* (2018) 'Chloroquine inhibits autophagic flux by decreasing autophagosome-lysosome fusion', *Autophagy*. Taylor & Francis, 14(8), pp. 1435–1455. doi: 10.1080/15548627.2018.1474314.

Meng, E. C. *et al.* (2023) 'UCSF ChimeraX: Tools for structure building and analysis', *Protein Science*, 32(11), pp. 1–13. doi: 10.1002/pro.4792.

Mi, H. *et al.* (2013) 'Large-scale gene function analysis with PANTHER Classification System', *Nature Protocols*, 8(8), pp. 1551–1566. doi: 10.1038/nprot.2013.092.

Morinaka, K. *et al.* (1999) ‘Epsin binds to the EH domain of POB1 and regulates receptor-mediated endocytosis’, *Oncogene*, 18(43), pp. 5915–5922. doi: 10.1038/sj.onc.1202974.

Narendra, D. P., Kane, L. A., *et al.* (2010) ‘p62/SQSTM1 is required for Parkin-induced mitochondrial clustering but not mitophagy; VDAC1 is dispensable for both’, *Autophagy*, 6(8), pp. 1090–1106. doi: 10.4161/auto.6.8.13426.

Narendra, D. P., Jin, S. M., *et al.* (2010) ‘PINK1 is selectively stabilized on impaired mitochondria to activate Parkin’, *PLoS Biology*, 8(1). doi: 10.1371/journal.pbio.1000298.

Narendra, D. P. and Youle, R. J. (2024) ‘The role of PINK1–Parkin in mitochondrial quality control’, *Nature Cell Biology*. Springer US, 26(October). doi: 10.1038/s41556-024-01513-9.

Nguyen, T. N. *et al.* (2023) ‘Article Unconventional initiation of PINK1 / Parkin mitophagy by Optineurin ll Unconventional initiation of PINK1 / Parkin mitophagy by Optineurin’, *Molecular Cell*. The Authors, 83(10), pp. 1693-1709.e9. doi: 10.1016/j.molcel.2023.04.021.

Nie, J. *et al.* (2024) ‘SEC31a-ATG9a Interaction Mediates the Recruitment of COPII Vesicles for Autophagosome Formation’, *Advanced Science*, 2405127, pp. 1–15. doi: 10.1002/advs.202405127.

Ordureau, A. *et al.* (2015) ‘Defining roles of PARKIN and ubiquitin phosphorylation by PINK1 in mitochondrial quality control using a ubiquitin replacement strategy’, *Proceedings of the National Academy of Sciences of the United States of America*, 112(21), pp. 6637–6642. doi: 10.1073/pnas.1506593112.

Ramella, M., Ribolla, L. M. and de Curtis, I. (2022) ‘Liquid–Liquid Phase Separation at the Plasma Membrane–Cytosol Interface: Common Players in Adhesion, Motility, and Synaptic Function’, *Journal of Molecular Biology*. Elsevier Ltd, 434(1), p. 167228. doi: 10.1016/j.jmb.2021.167228.

Rappsilber, J., Mann, M. and Ishihama, Y. (2007) ‘Protocol for micro-purification, enrichment, pre-fractionation and storage of peptides for proteomics using StageTips’, *Nature Protocols*, 2(8), pp. 1896–1906. doi: 10.1038/nprot.2007.261.

Richter, B. *et al.* (2016) ‘Phosphorylation of OPTN by TBK1 enhances its binding to Ub chains and promotes selective autophagy of damaged mitochondria’, *Proceedings of the National Academy of Sciences of the United States of America*, 113(15), pp. 4039–4044. doi: 10.1073/pnas.1523926113.

Rose, C. M. *et al.* (2016) ‘Highly Multiplexed Quantitative Mass Spectrometry Analysis of

Ubiquitylomes', *Cell Systems*. Elsevier Inc., 3(4), pp. 395-403.e4. doi: 10.1016/j.cels.2016.08.009.

Sarraf, S. A. *et al.* (2013) 'Landscape of the PARKIN-dependent ubiquitylome in response to mitochondrial depolarization', *Nature*. Nature Publishing Group, 496(7445), pp. 372–376. doi: 10.1038/nature12043.

Sharma, K. *et al.* (2024) 'A Novel PINK1 p.F385S Loss-of-Function Mutation in an Indian Family with Parkinson's Disease', *Movement Disorders*, 39(7), pp. 1217–1225. doi: 10.1002/mds.29792.

Shiba-Fukushima, K. *et al.* (2012) 'PINK1-mediated phosphorylation of the Parkin ubiquitin-like domain primes mitochondrial translocation of Parkin and regulates mitophagy', *Scientific Reports*, 2, pp. 1–8. doi: 10.1038/srep01002.

Stankewich, M. C., Stabach, P. R. and Morrow, J. S. (2006) 'Human Sec31B: A family of new mammalian orthologues of yeast Sec31p that associate with the COPII coat', *Journal of Cell Science*, 119(5), pp. 958–969. doi: 10.1242/jcs.02751.

Stirling, D. R. *et al.* (2021) 'CellProfiler 4: improvements in speed, utility and usability', *BMC Bioinformatics*. BioMed Central, 22(1), pp. 1–11. doi: 10.1186/s12859-021-04344-9.

Tumbarello, D. A. *et al.* (2012) 'Autophagy receptors link myosin VI to autophagosomes to mediate Tom1-dependent autophagosome maturation and fusion with the lysosome', *Nature Cell Biology*. Nature Publishing Group, 14(10), pp. 1024–1035. doi: 10.1038/ncb2589.

Turco, E. *et al.* (2021) 'Reconstitution defines the roles of p62, NBR1 and TAX1BP1 in ubiquitin condensate formation and autophagy initiation', *Nature Communications*. Springer US, 12(1), pp. 1–16. doi: 10.1038/s41467-021-25572-w.

Tyanova, S. *et al.* (2016) 'The Perseus computational platform for comprehensive analysis of (prote)omics data', *Nature Methods*, 13(9), pp. 731–740. doi: 10.1038/nmeth.3901.

Wang, J. *et al.* (2017) 'Autophagosome formation: Where the secretory and autophagy pathways meet', *Autophagy*. Taylor & Francis, 13(5), pp. 973–974. doi: 10.1080/15548627.2017.1287657.

Wartosch, L. *et al.* (2015) 'Recruitment of VPS33A to HOPS by VPS16 Is Required for Lysosome Fusion with Endosomes and Autophagosomes', *Traffic*, 16(7), pp. 727–742. doi: 10.1111/tra.12283.

1013 Waterhouse, A. M. *et al.* (2009) 'Jalview Version 2-A multiple sequence alignment editor
1014 and analysis workbench', *Bioinformatics*, 25(9), pp. 1189–1191. doi:
1015 10.1093/bioinformatics/btp033.

1016 Yamano, K. *et al.* (2014) 'Mitochondrial Rab GAPs govern autophagosome biogenesis
1017 during mitophagy', *eLife*, 3, pp. 1–24. doi: 10.7554/elife.01612.

1018 Yamano, K. *et al.* (2018) 'Endosomal Rab cycles regulate Parkin- mediated mitophagy',
1019 pp. 1–32.

1020 Yamano, K. *et al.* (2020) 'Critical role of mitochondrial ubiquitination and the OPTN ATG9A
1021 axis in mitophagy', *Journal of Cell Biology*, 219(9). doi: 10.1083/jcb.202001120.

1022 Yamano, K. *et al.* (2024) 'Optineurin provides a mitophagy contact site for TBK1
1023 activation', *EMBO Journal*. Springer US, 43(5), pp. 754–779. doi: 10.1038/s44318-024-
1024 00036-1.

1025 Zellner, S., Schifferer, M. and Behrends, C. (2021) 'Systematically defining selective
1026 autophagy receptor-specific cargo using autophagosome content profiling', *Molecular Cell*.
1027 Elsevier, 81(6), pp. 1337-1354.e8. doi: 10.1016/j.molcel.2021.01.009.

1028 Zhao, Y. G., Codogno, P. and Zhang, H. (2021) 'Machinery, regulation and
1029 pathophysiological implications of autophagosome maturation', *Nature Reviews Molecular
1030 Cell Biology*. Springer US, 22(11), pp. 733–750. doi: 10.1038/s41580-021-00392-4.

1031 Zittlau, K. I. *et al.* (2022) 'Temporal Analysis of Protein Ubiquitylation and Phosphorylation
1032 During Parkin-Dependent Mitophagy', *Molecular and Cellular Proteomics*. The Authors,
1033 21(2), p. 100191. doi: 10.1016/j.mcpro.2021.100191.

Figure 1

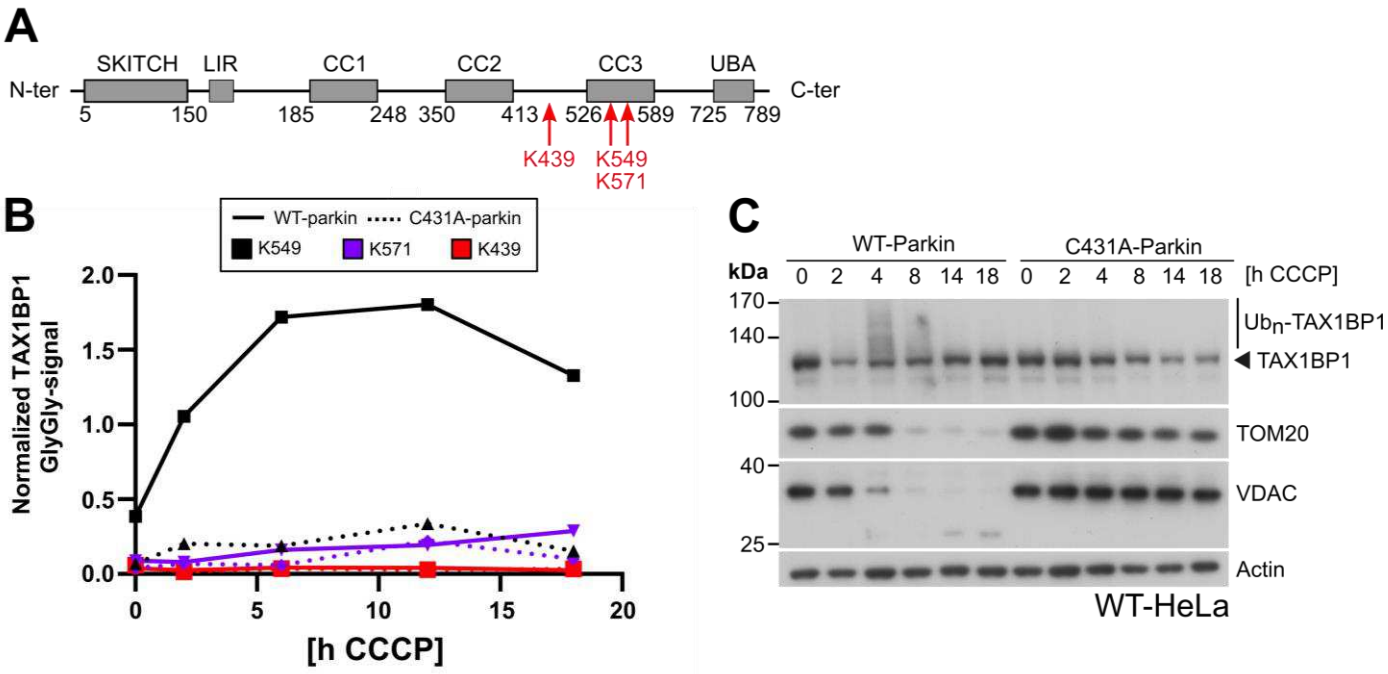


Figure 1: Ubiquitination of TAX1BP1 upon CCCP-induced mitophagy in HeLa cells stably expressing WT- or C431A-Parkin. (A) Schematic representation of TAX1BP1 domain structure. Identified ubiquitinated lysine residues from the ubiquitylome mass-spectrometry screen are indicated in red. **(B)** Normalized Gly-Gly peptide signals of the identified ubiquitinated residues in both WT- and C431A-parkin HeLa cell lines during mitophagy induction at the indicated time-points. **(C)** Western blot detection of the indicated proteins in whole cell lysates from HeLa cells stably expressing WT- or catalytically inactive C431A-parkin treated with CCCP for the indicated times. TAX1BP1 band shift peaking at 4h confirms ubiquitination.

Figure 2

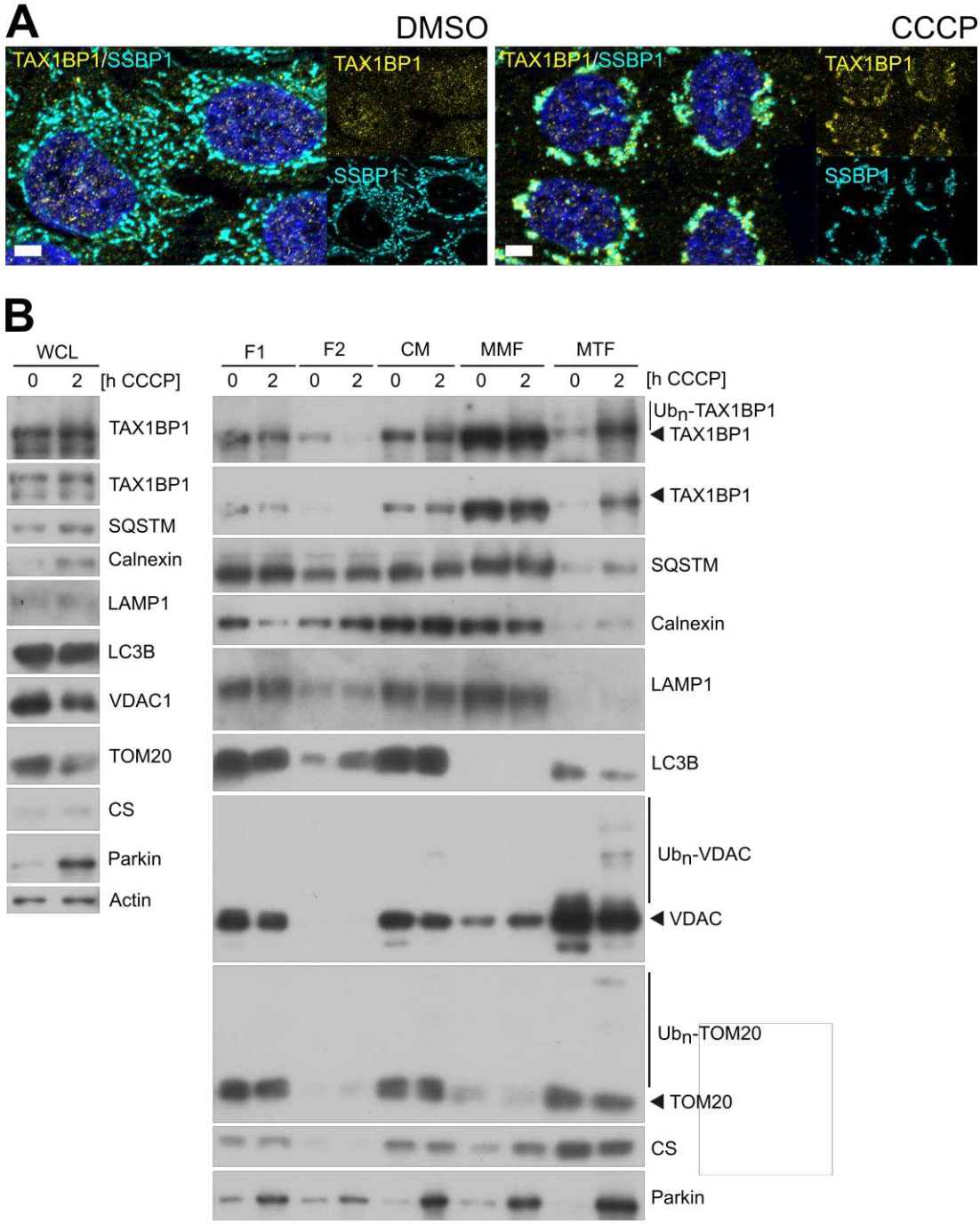


Figure 2: TAX1BP1 translocation to mitochondria during CCCP-induce mitophagy. (A) Representative immunofluorescence images showing endogenous TAX1BP1 (yellow), and the inner mitochondrial marker SSBP1 (cyan) at basal levels or after mitophagy induction (10 µM CCCP, 2h). Scale bars: 5 µm **(B)** Subcellular fractionation of WT-Parkin HeLa cells under basal conditions or after short depolarization, where translocation of parkin and ubiquitinated TAX1BP1 to mitochondria can be observed. WCL: whole cell lysate, F1: fraction 1, F2: fraction 2, CM: crude mitochondria fraction, MMF: membrane enriched fraction, MTF: mitochondrial enriched fraction.

Figure 3

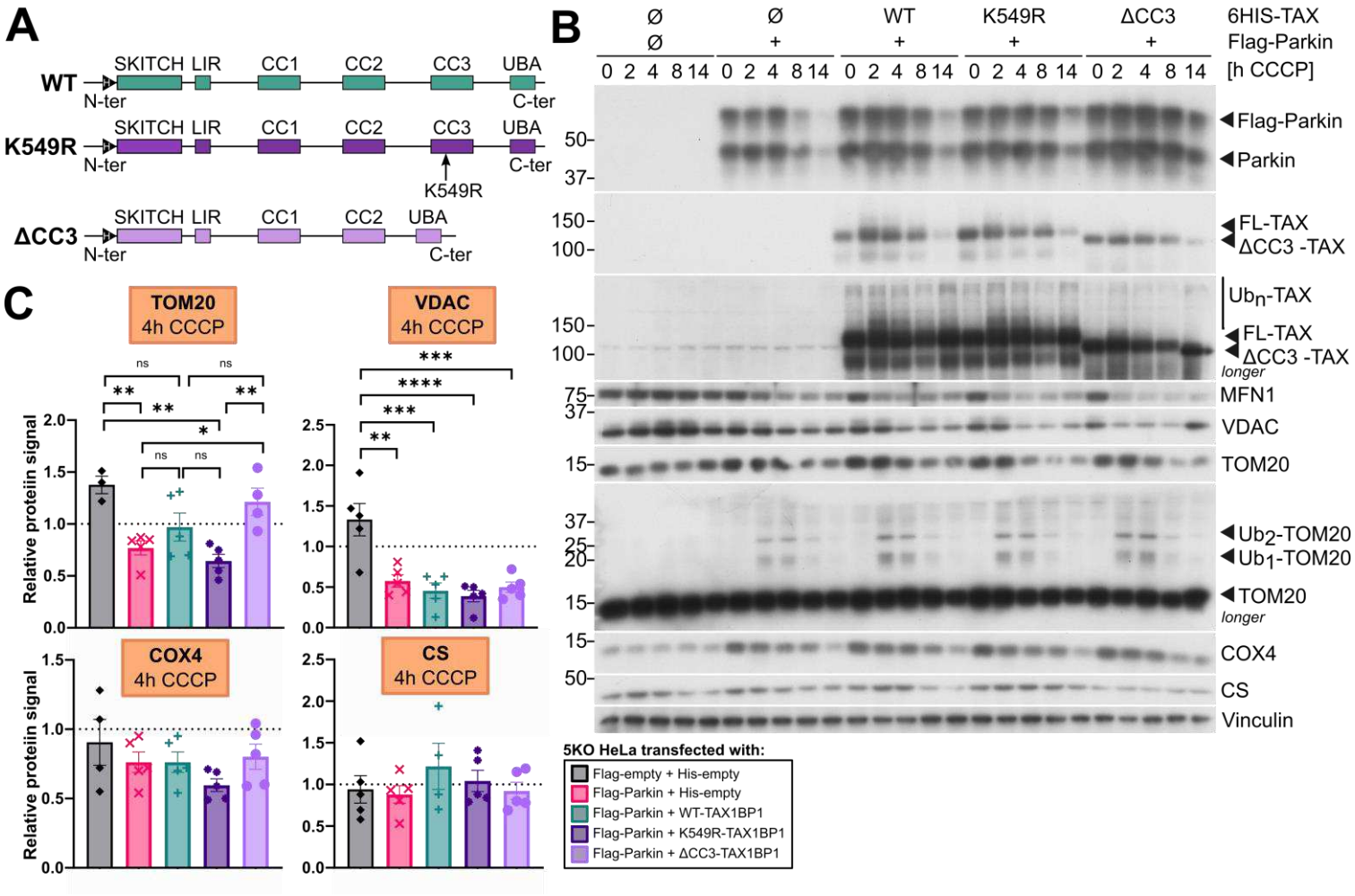


Figure 3: Over-expression of TAX1BP1 WT-, K549R- and ΔCC3- leads to changes in its ubiquitination pattern and has mild effects on mitochondrial protein turnover. (A) Schematic representation of the HIS-tagged TAX1BP1 constructs harbouring residue-specific or deletion mutations at the CC3 domain. H: 6xHis-tag **(B)** Mitophagy timecourse in 5KO-HeLa cells transiently expressing WT-, K549R- and ΔCC3-TAX1BP1 with or without Flag-tagged WT-Parkin co-transfection. Ø: empty control plasmids. **(C)** Mitochondrial protein quantification from experiments as shown in (B). Data of at least three independent experiments. Protein signal ratios were obtained after normalization of protein signal with loading control (vinculin) and subsequent normalization with protein values at basal level. Bars: Mean ± SEM.

Figure 4

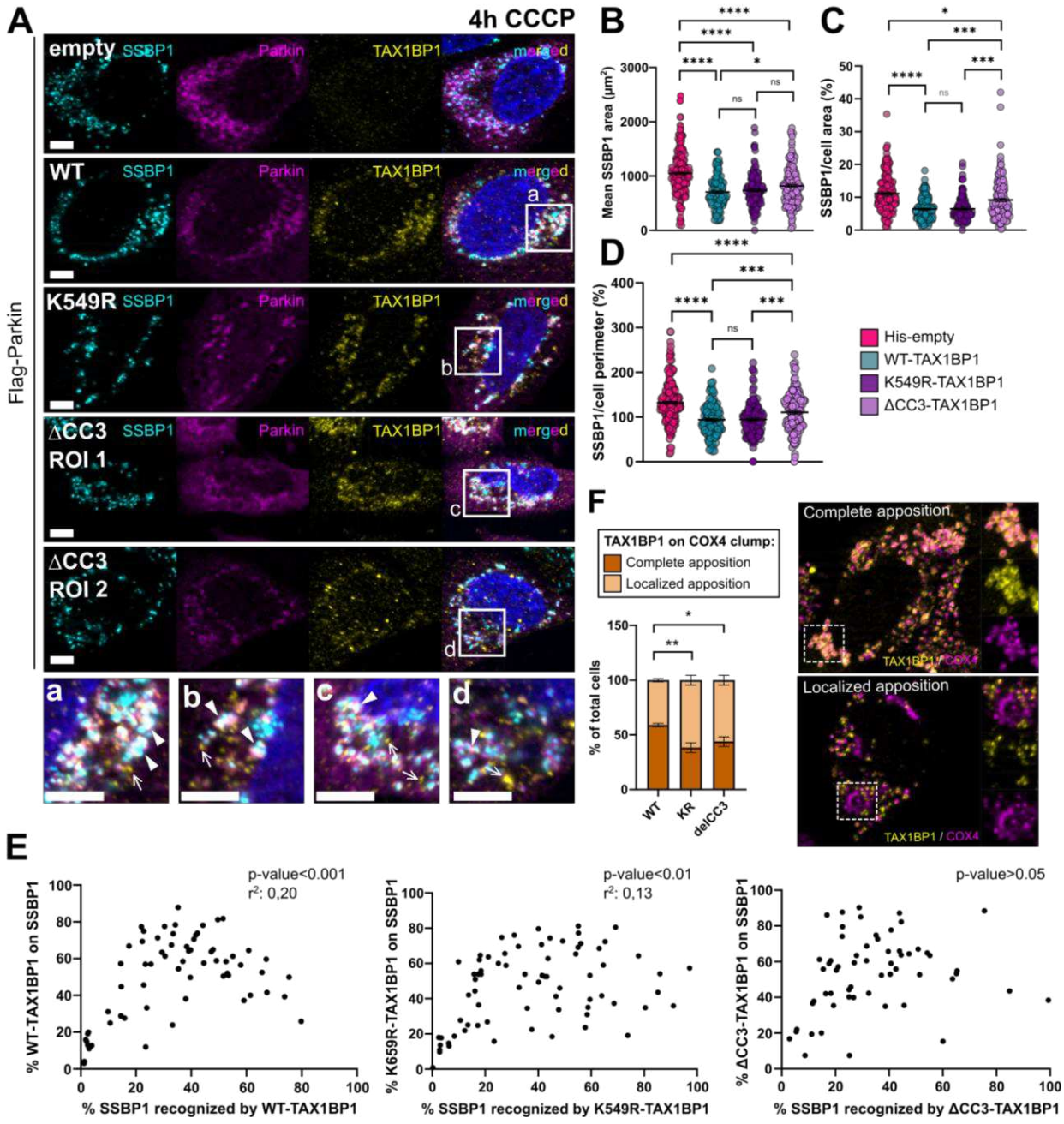


Figure 4: Single cell analysis of TAX1BP1 translocation to mitochondria after CCCP-mediated depolarization. (A) Representative immunofluorescence images showing TAX1BP1 (yellow), parkin (magenta) and SSBP1 (cyan) after mitochondria depolarization in 5KO HeLa cells. Solid arrowheads indicate TAX1BP1 structures co-localizing with mitochondrial material. Arrows indicate TAX1BP1 structures not engaged with mitochondrial material. ROI 1 represents > 50 % of cell population while ROI 2 represents < 50% of cases. Scale bars: 10 µm. **(B)** Mean mitochondrial size of SSBP1 foci after 4h CCCP. **(C-D)** Normalized SSBP1 (C) area or (D) perimeter per cell. **(E)** Correlation analysis of the percentage of mitochondrial area recognized by TAX1BP1 (X axis) in relation to the percentage of total TAX1BP1 found on mitochondria (Y axis). Significance p-values are indicated in the graph for the indicated TAX1BP1 constructs. **(F)** Left panel: quantitative analysis of WT-,

K549R- or ΔCC3-TAX1BP1 localization after mitochondria depolarization in 5KO-PRKN cells after mitophagy induction (4h CCCP). TAX1BP1 localization is classified between cells where COX4 clumps are fully recognized by TAX1BP1 (complete apposition) and cells where COX4 clumps recognition is limited (localized apposition). Bars: mean ± SEM. Right panel: representative immunofluorescence images stained for TAX1BP1 (yellow) and COX4 (magenta) are shown for each category.

Figure 5

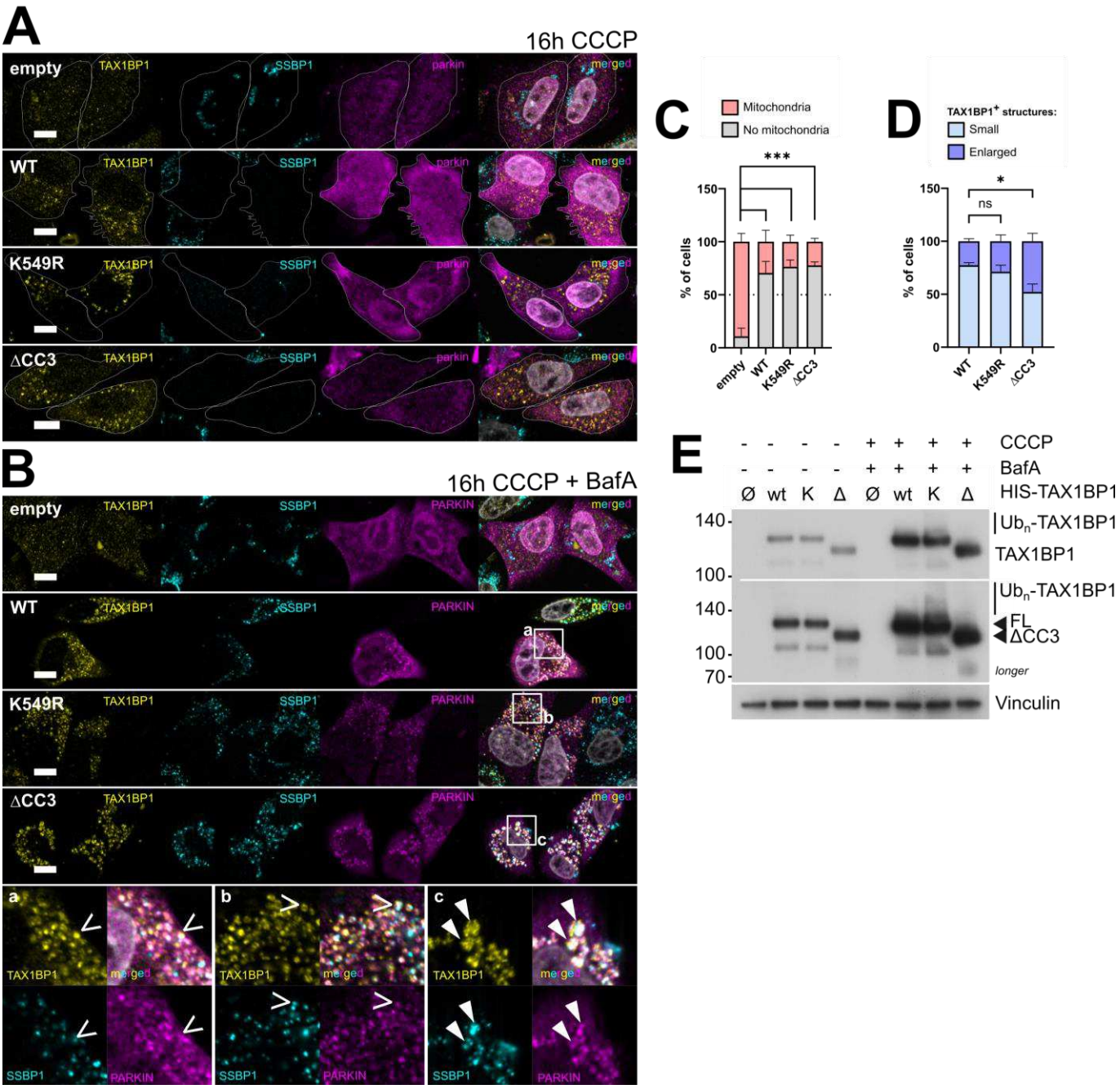


Figure 5: Autophagy flux blockage effects in 5KO-PARK HeLa cells. (A-B) Representative immunofluorescence images of 5KO-PARK HeLa cells showing TAX1BP1 (yellow), parkin (magenta) and SSBP1 (cyan) after mitochondria depolarization only (A) or with Bafilomycin A (BafA) (B). In (A), cells with no remaining SSBP1 material are highlighted. In (B), solid arrowheads indicate enlarged TAX1BP1/SSBP1-positive puncta while thin arrowheads indicate small TAX1BP1/SSBP1-positive puncta. **(C-D)** Eye-based quantification of (C) cell percentage with remaining SSBP1 material after extended CCCP treatment and (D) cells harboring enlarged or small TAX1BP1 puncta positive for SSBP1. Scale bars: 10 µm. **(E)** Changes in TAX1BP1 ubiquitination after 16 h of CCCP treatment combined with BafA.

Figure 6

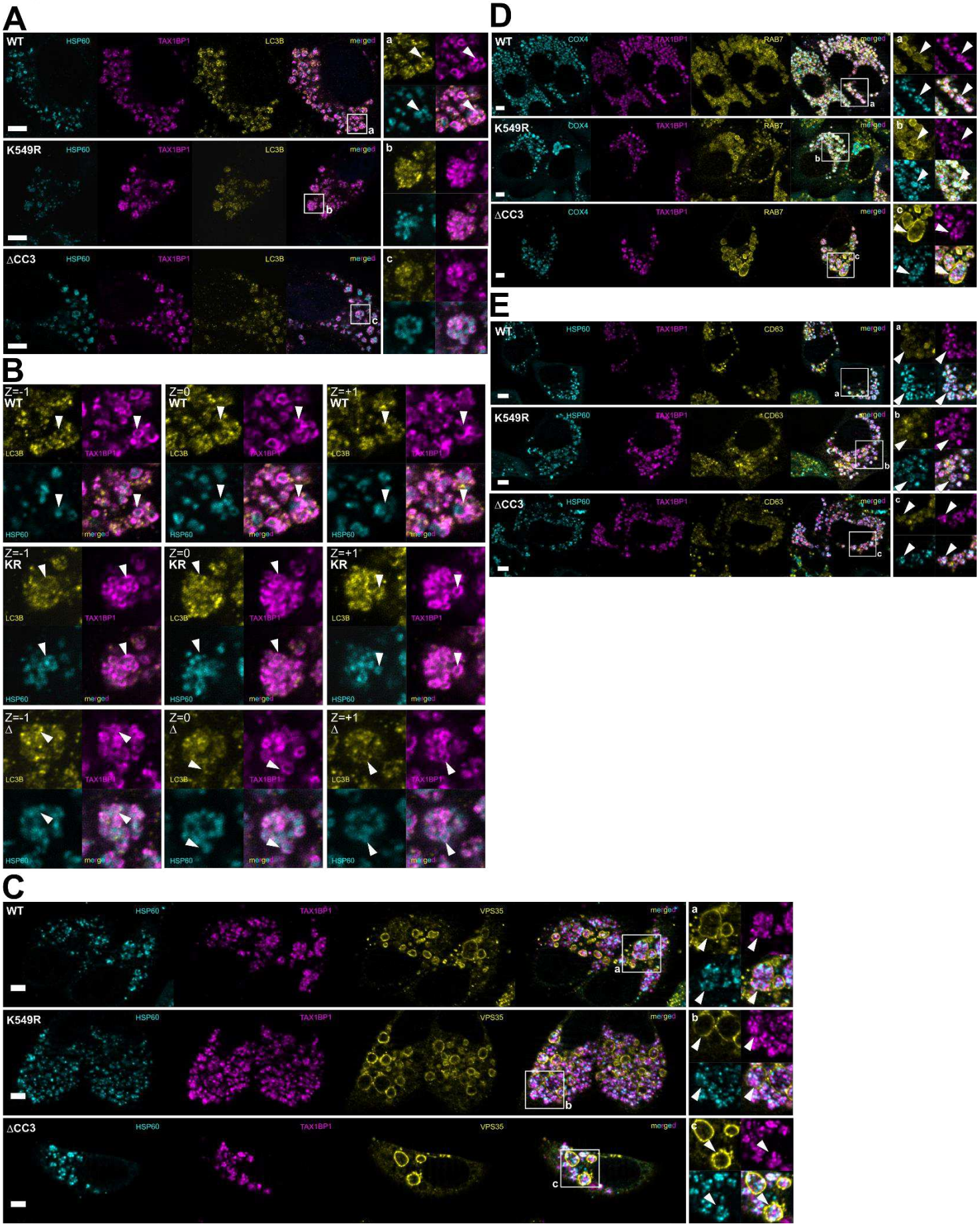

A
WT
HSP60
TAX1BP1
LC3B
merged
K549R
ΔCC3
B
Z=-1
Z=0
Z=+1
WT
KR
Δ
C
VPS35
D
COX4
RAB7
E
CD63

Figure 6: Characterization of enlarged TAX1BP1-positive vesicles carrying mitochondrial material upon autophagy flux inhibition in 5KO-PARK. (A) Representative images of 5KO-PARK HeLa cells showing enlarged TAX1BP1/HSP60-positive structures (magenta, cyan) positive for the autophagosome marker LC3B (yellow) after mitochondria depolarization and BafA for 16h. Scale bars: 5 μm. **(B)** Z-stack projection of enlarged vesicles identified in (A) for WT, K549R and ΔCC3-TAX1BP1. Thick arrowheads indicate LC3B/TAX1BP1-positive cup-shaped structures in each Z-plane. Thickness slice: 0.6 μm. **(C-E)** Representative images showing enlarged TAX1BP1/HSP60-positive structures positive for the RAB7 (C), VPS35 (D) and CD63 (E). Scale bars: 5 μm.

Figure 7

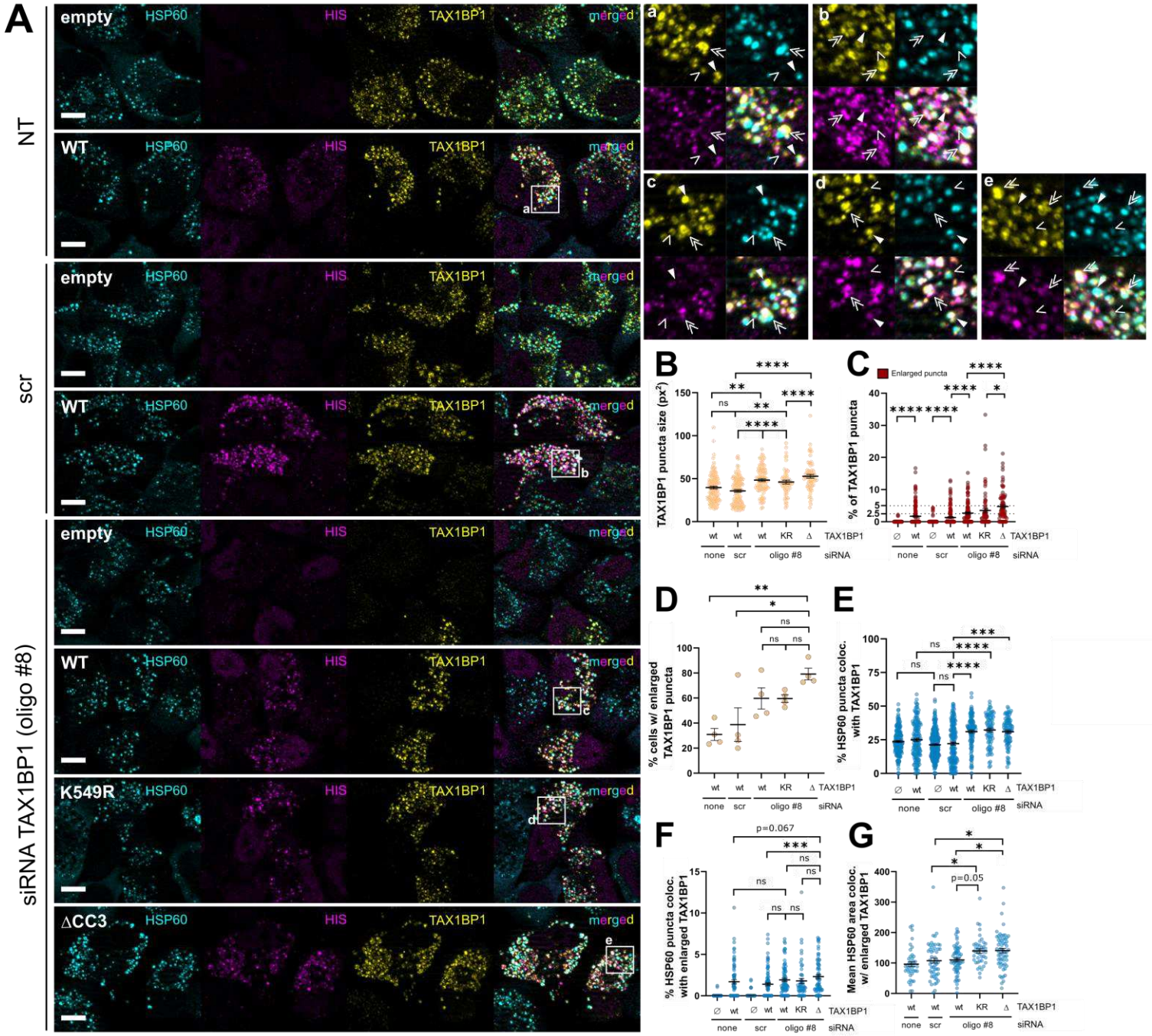


Figure 7: Characterization of TAX1BP1-positive structures identified in WT-Parkin Hela cells upon autophagy flux inhibition. (A) Representative images upon siRNA mediated knock-down of TAX1BP1 in WT-Parkin HeLa cells showing TAX1BP1-positive structures (magenta) carrying mitochondrial material (HSP60, cyan). Scale bars: 10 μm. **(B-G)** CellProfiler based analysis of TAX1BP1 puncta size (B-D) or HSP60 material colocalizing with TAX1BP1 puncta (E-G) in WT-PARK HeLa cells after siRNA mediated TAX1BP1 knockdown and TAX1BP1 re-transfection upon CCCP and BafA treatment. **(B)** Mean TAX1BP1-positive structures size. **(C)** Percentage of enlarged TAX1BP1 structures. **(D)** Percentage of total cells harboring enlarged TAX1BP1-positive structures. **(E)** Percentage of HSP60 foci colocalizing with TAX1BP1. **(F)** Percentage of HSP60 colocalizing with enlarged TAX1BP1-positive structures. **(G)** Mean HSP60 foci area colocalizing with enlarged TAX1BP1-positive structures.

Figure 8

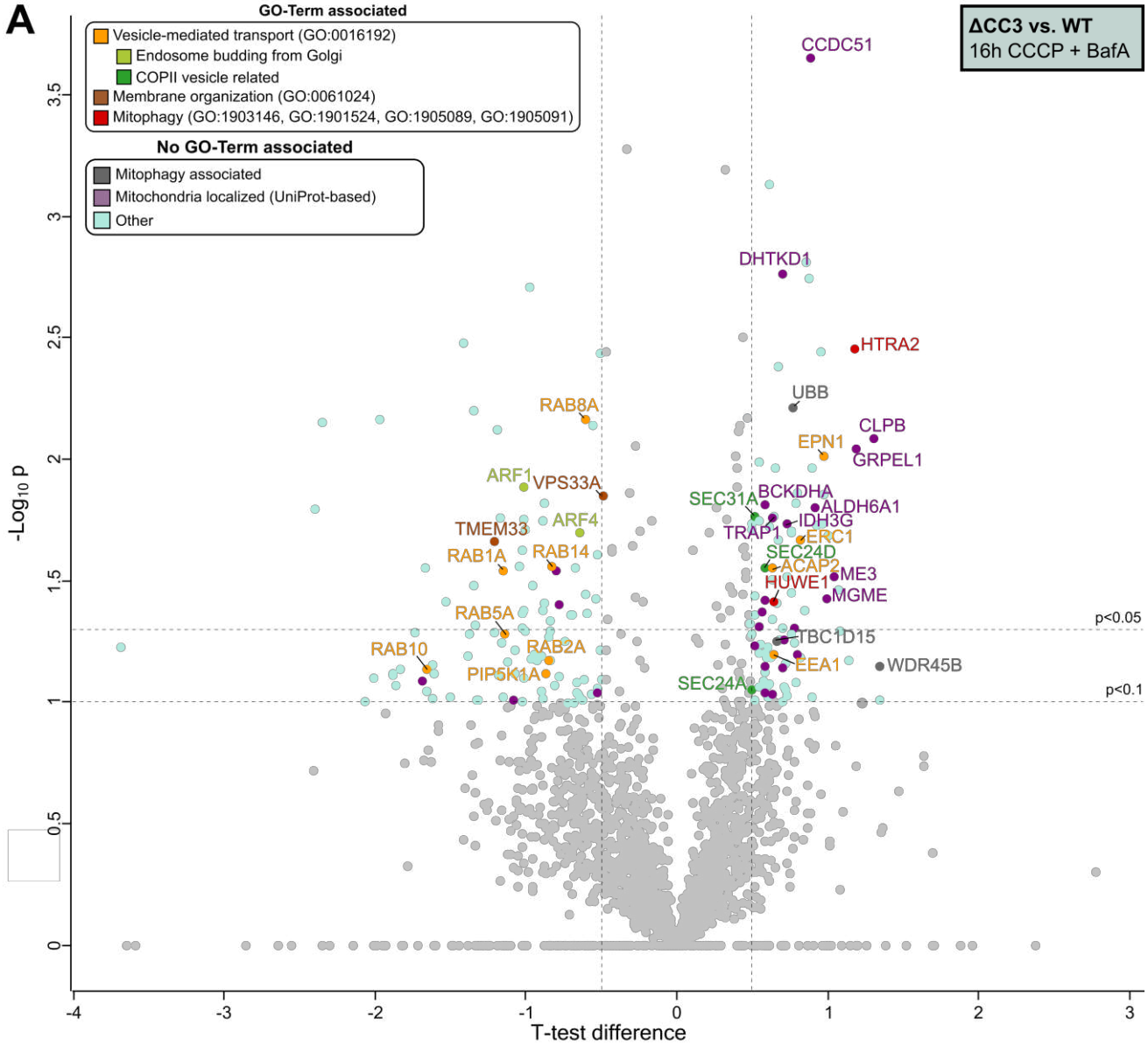
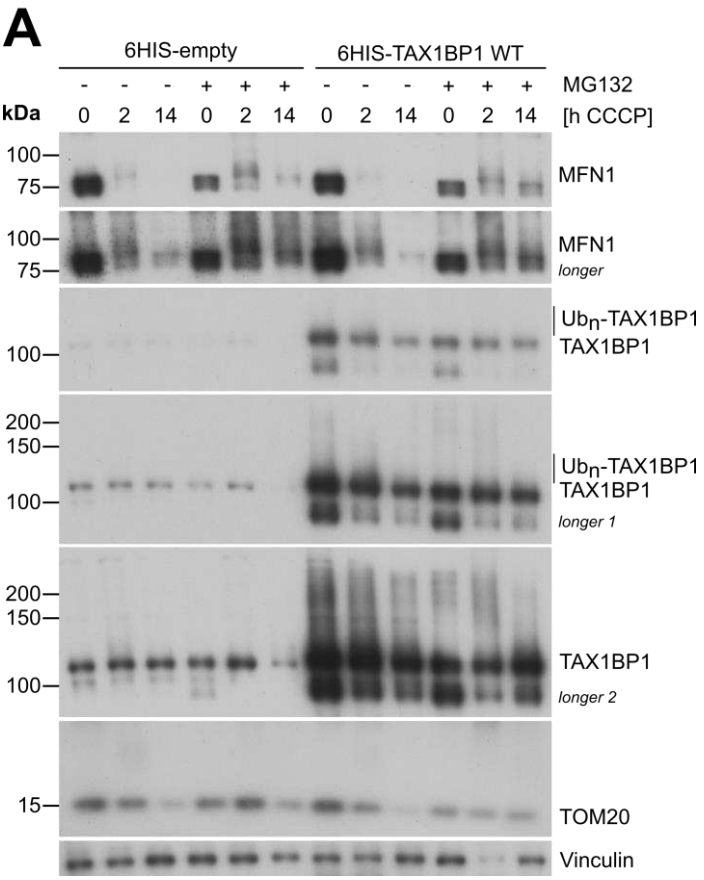

A
GO-Term associated
Vesicle-mediated transport (GO:0016192)
Endosome budding from Golgi
COPII vesicle related
Membrane organization (GO:0061024)
Mitophagy (GO:1903146, GO:1901524, GO:1905089, GO:1905091)
No GO-Term associated
Mitophagy associated
Mitochondria localized (UniProt-based)
Other
ΔCC3 vs. WT
16h CCCP + BafA
CCDC51
DHTKD1
HTRA2
UBB
CLPB
EPN1
GRPEL1
RAB8A
ARF1
VPS33A
SEC31A
BCKDHA
ALDH6A1
IDH3G
TRAP1
ERC1
SEC24D
ACAP2
ME3
HUWE1
MGME
TMEM33
ARF4
RAB1A
RAB14
RAB5A
RAB10
RAB2A
PIP5K1A
TBC1D15
EEA1
WDR45B
SEC24A
p<0.05
p<0.1
-Log10 p
T-test difference
B
ΔCC3 vs. WT
down
up
organic acid metabolic process
DNA metabolic process
DNA repair
dsDNA break repair via break−induced replication
DNA replication
regulation of DNA replication
DNA conformation change
mRNA 3'−splice site recognition
U2−type prespliceosome assembly
response to mitochondrial depolarization
positive regulation of mitophagy
protein transport
vesicle−mediated transport
nuclear transport
nucleocytoplasmic transport
membrane organization
vesicle organization
vesicle localization
vesicle budding from membrane
membrane fusion
Golgi vesicle transport
ER to Golgi vesicle−mediated transport
positive regulation of telomerase RNA loc. to Cajal body
mitochondrial ADP transmembrane transport
−LOG10 P−value
LOG2 fold enrichment

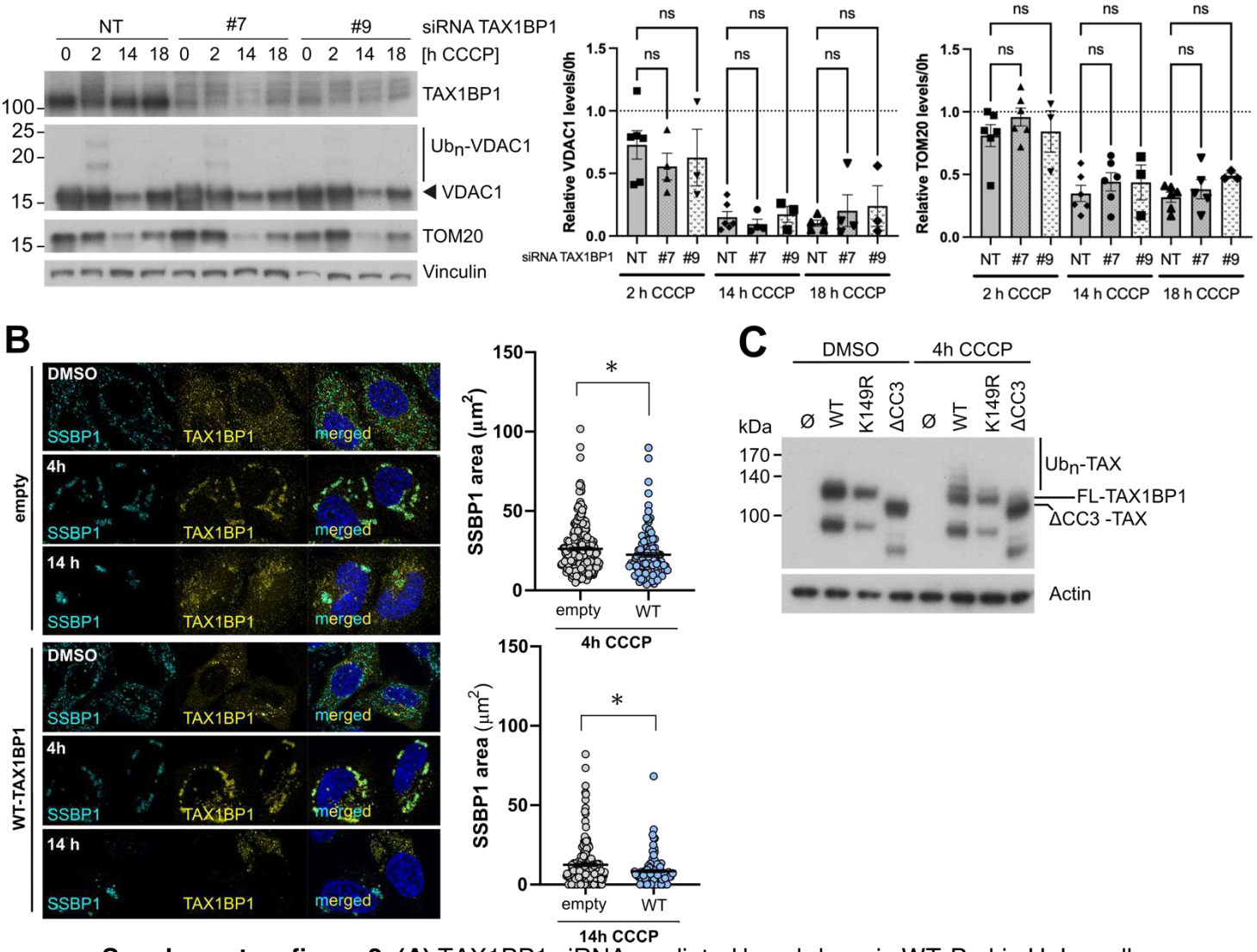
Figure 8: Mass spectrometry analysis of TAX1BP1 native pulldown indicates defects in protein trafficking processes in ΔCC3-TAX1BP1. (A) Overrepresentation analysis of biological processes for significantly regulated proteins by Fisher exact testing. **(B)** Statistical analysis of ΔCC3 vs. WT TAX1BP1 pulldowns represented by the $\log_{10}$ p-value plotted against student's T-test difference. Significance lines represent $p \leq 0.05$ and $p \leq 0.1$, as indicated. Proteins are grouped according to the following GO-Terms: vesicle-mediated transport in orange (GO:0016192), membrane organization in brown (GO:0061024) and mitophagy in red (GO:1903146; GO:1901524; GO:1905089; GO:1905091); mitochondria localization in lila (based on UniProt annotation) or if they are associated with PINK1/parkin mitophagy in grey (based on literature). Proteins related to the GO-Term vesicle-mediated transport (GO:0016192) are classified according to their functionality (based on UniProt and literature); between endosome budding from Golgi (light green) or COPII vesicle related (dark green).

Supplementary Figure 1



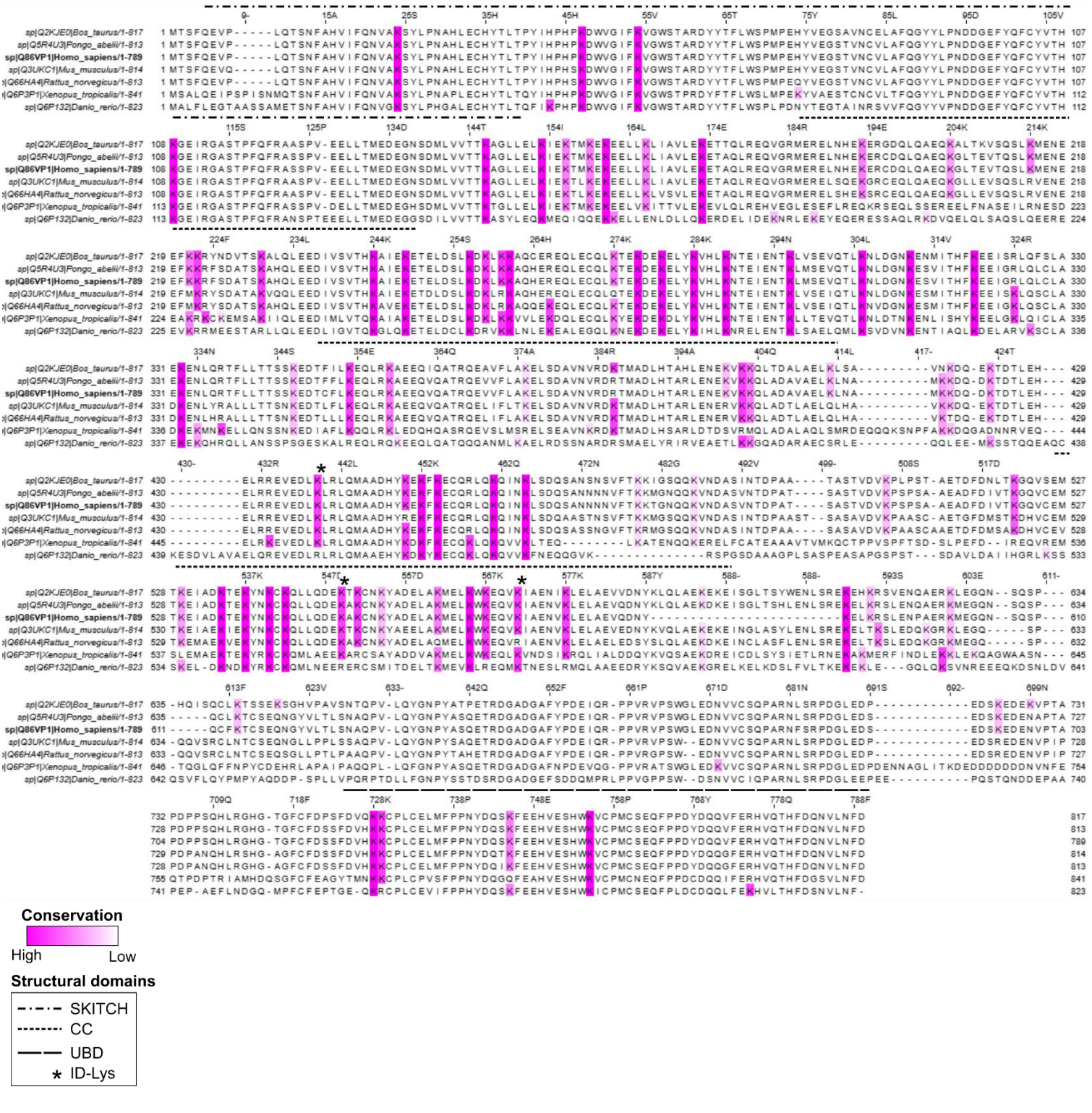
Supplementary Figure 1: TAX1BP1 ubiquitination does not direct the autophagy adaptor to proteasomal degradation. WT-Parkin HeLa cells were transfected with HIS-tagged TAX1BP1 and subjected to mitochondrial depolarization for the indicated timepoints, in the presence (+) or absence (-) of the proteasomal inhibitior MG132. Mitophagy was confirmed by probing for the immediate-early protasome substrate MFN1 and the later autophagy substrate TOM20. Vinculin served as loading control.

Supplementary Figure 2



Supplementary figure 2: (A) TAX1BP1 siRNA mediated knockdown in WT-Parkin HeLa cells does not impair VDAC and TOM20 degradation upon acute mitochondria depolarization. WT-Parkin HeLa cells were transfected with siRNA against TAX1BP1 for three consecutive days. After the third day, mitochondria were depolarized with CCCP for the indicated time-points and protein quantification was performed. **(B)** WT-Parkin HeLa cells were transfected with His-tagged TAX1BP1 for 24h. Further, mitochondria were depolarized with 10 µm CCCP for the indicated time-points. Left panel: Representative immunofluorescence images showing SSBP1 (cyan) and TAX1BP1 (yellow) upon mock or HIS-TAX1BP1 transfection after CCCP-mediated depolarization at the indicated time-points. Right panel: Reduction of SSBP1 area after TAX1BP1 transfection after short (4h) or extended (14h) CCCP treatment. Scale bars: 5 µm. **(C)** Changes in ubiquitination pattern of His-tagged TAX1BP1 after 4h CCCP in 5KO-PARK HeLa cells.

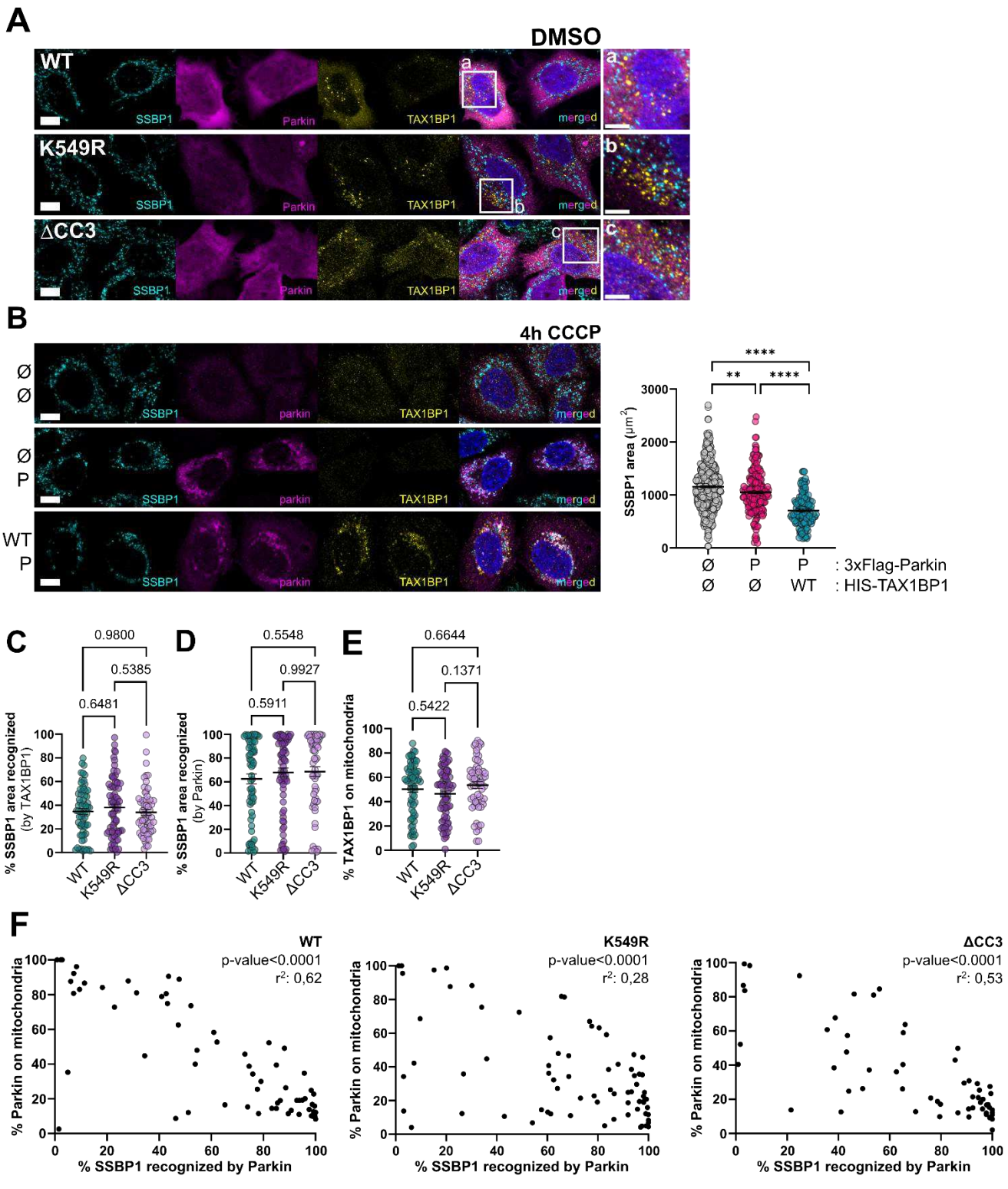
Supplementary figure 3



Supplementary Figure 3: TAX1BP1 alignment across species with emphasis on lysine conservation. (A) TAX1BP1 sequences from human (*Homo sapiens*), cow (*Bos Taurus*), orang-utan (*Pongo abelii*), mice (*Mus musculus*), rat (*Rattus norvegicus*), frog (*Xenopus tropicalis*) and zebrafish (*Danio rerio*) were aligned using the online tool MAFFT (https://mafft.cbrc.jp/alignment/server/index.html) and the software JalviewJS (Version 2.11.4.1) was used for visualization and lysine conservation analysis (Waterhouse *et al.*, 2009; Katoh, Rozewicki and Yamada, 2018). All lysine residues are shown in magenta across all

TAX1BP1 species. (*) Identified lysines in the mass-spectrometry screen. Structural domains are indicated with the indicated symbol lines. Lysine conservation analysis was performed with JalviewJS software, using the conservation colour increment function with a threshold of 25.

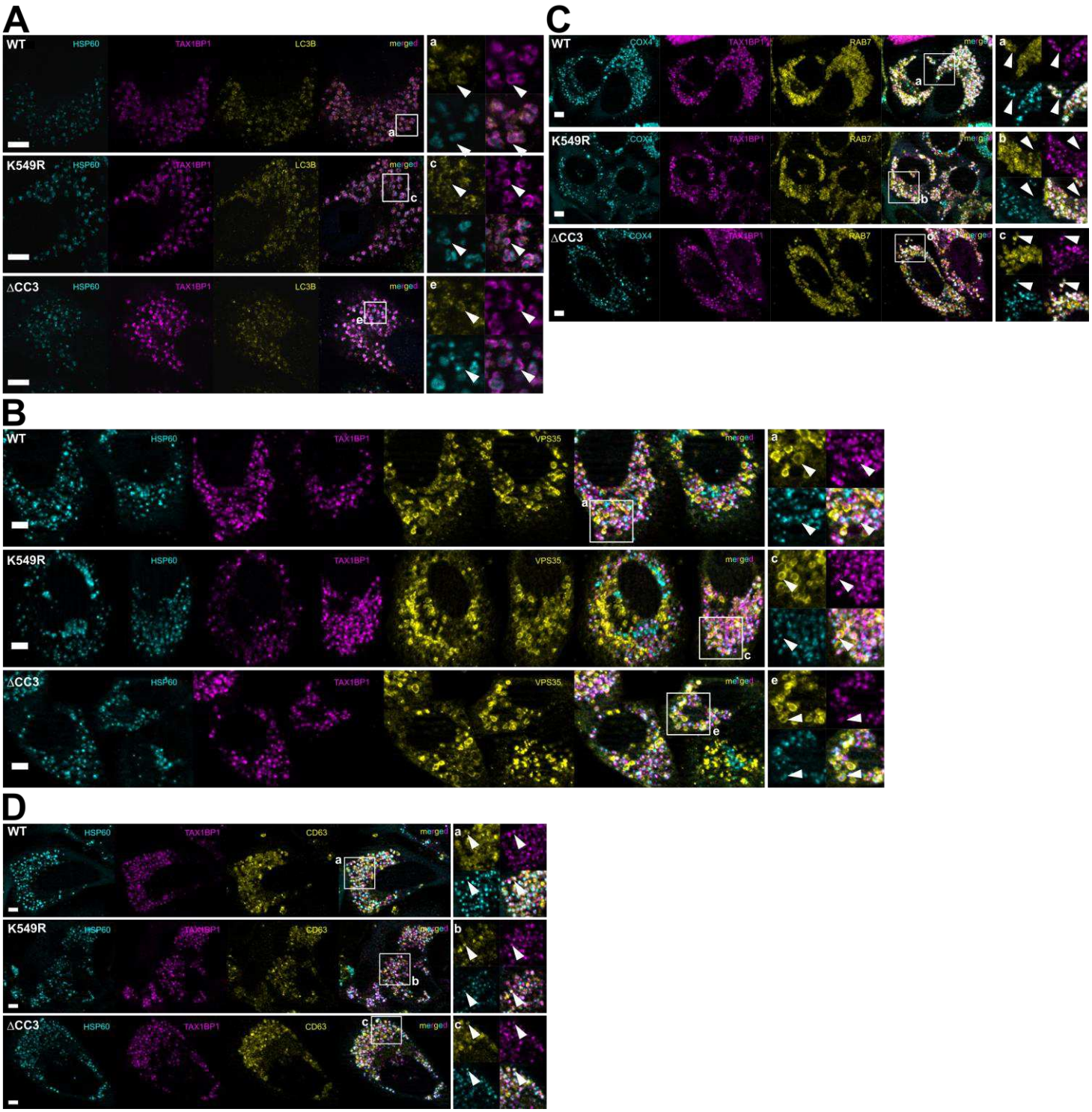
Supplementary Figure 4



Supplementary figure 4: (A) Overexpression of HIS-tagged WT-, K549R, ΔCC3-TAX1BP1 (yellow) in 5KO-HeLa cells co-transfected with Flag-parkin (magenta). Mitochondria are stained with SSBP1 (cyan). Scale bars: 10 µm. **(B)** Left panel shows representative images of 5KO-HeLa cells stained for SSBP1 (cyan), overexpressing Flag-parkin (P, magenta) and His-tagged WT-TAX1BP1 (WT, yellow). Cells were treated with 10 µM CCCP for 4 hours. Right panel shows Cell-Profiler based quantification of mitochondrial area represented by SSBP1. Ø: empty plasmid. P: 3xFlag-Parkin co-transfection. Scale bars: 10 µm. **(C-F)** Cell-profiler

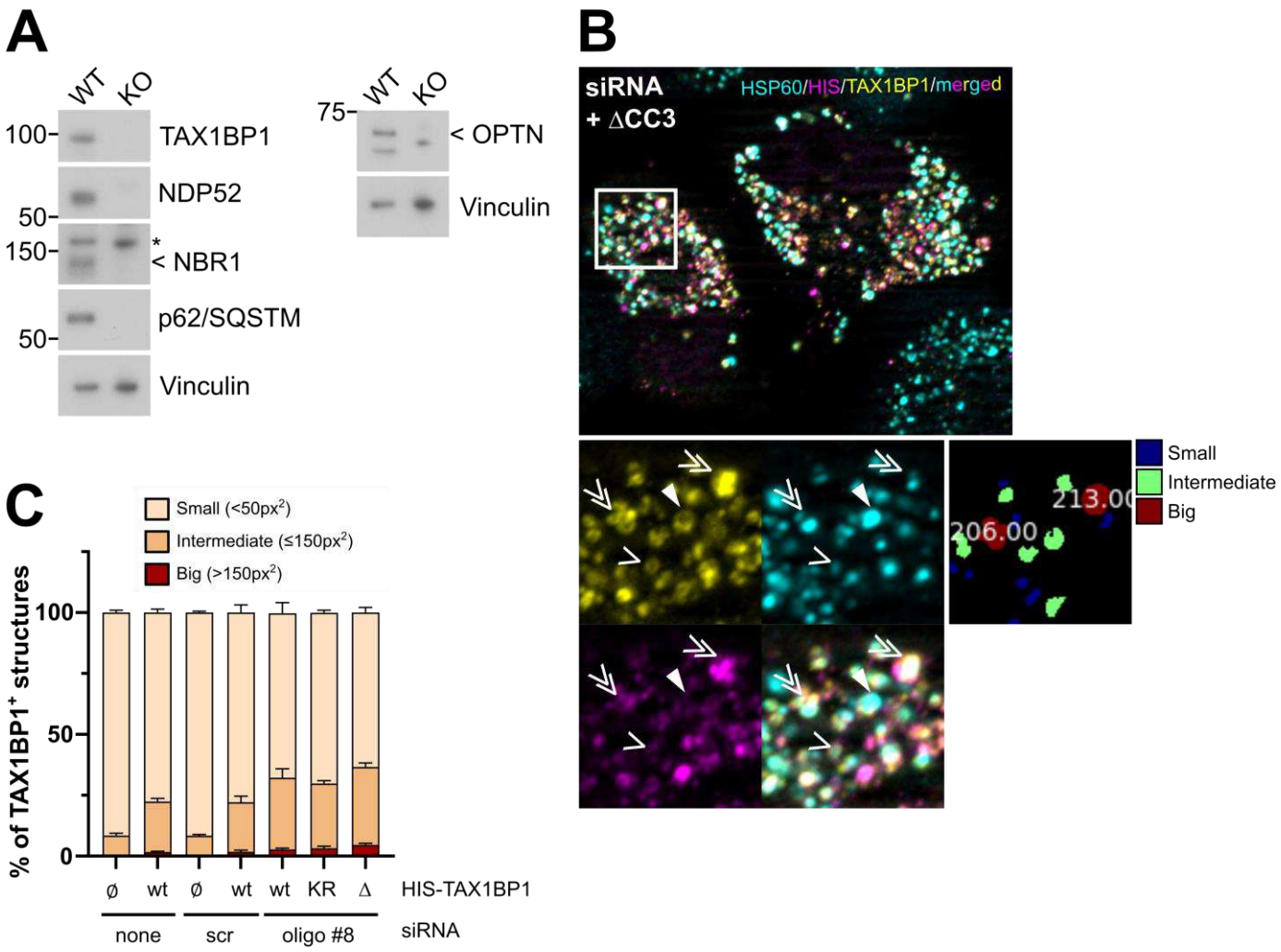
based quantification of several parameters of 5KO HeLa cells co-transfected with Flag-parkin and TAX1BP1 (WT and mutants) after 4h CCCP. **(C-D)** Percentage of SSBP1 area recognized by **(C)** TAX1BP1 and **(D)** Parkin. **(E)** Percentage of TAX1BP1 found on mitochondria after 4h CCCP. **(F)** Pearson correlation analysis of the percentage of translocated parkin (Y) and the percentage of SSBP1 area recognized (X) in cells co-transfected with WT-, K549R- and ΔCC3-TAX1BP1.

Supplementary Figure 5



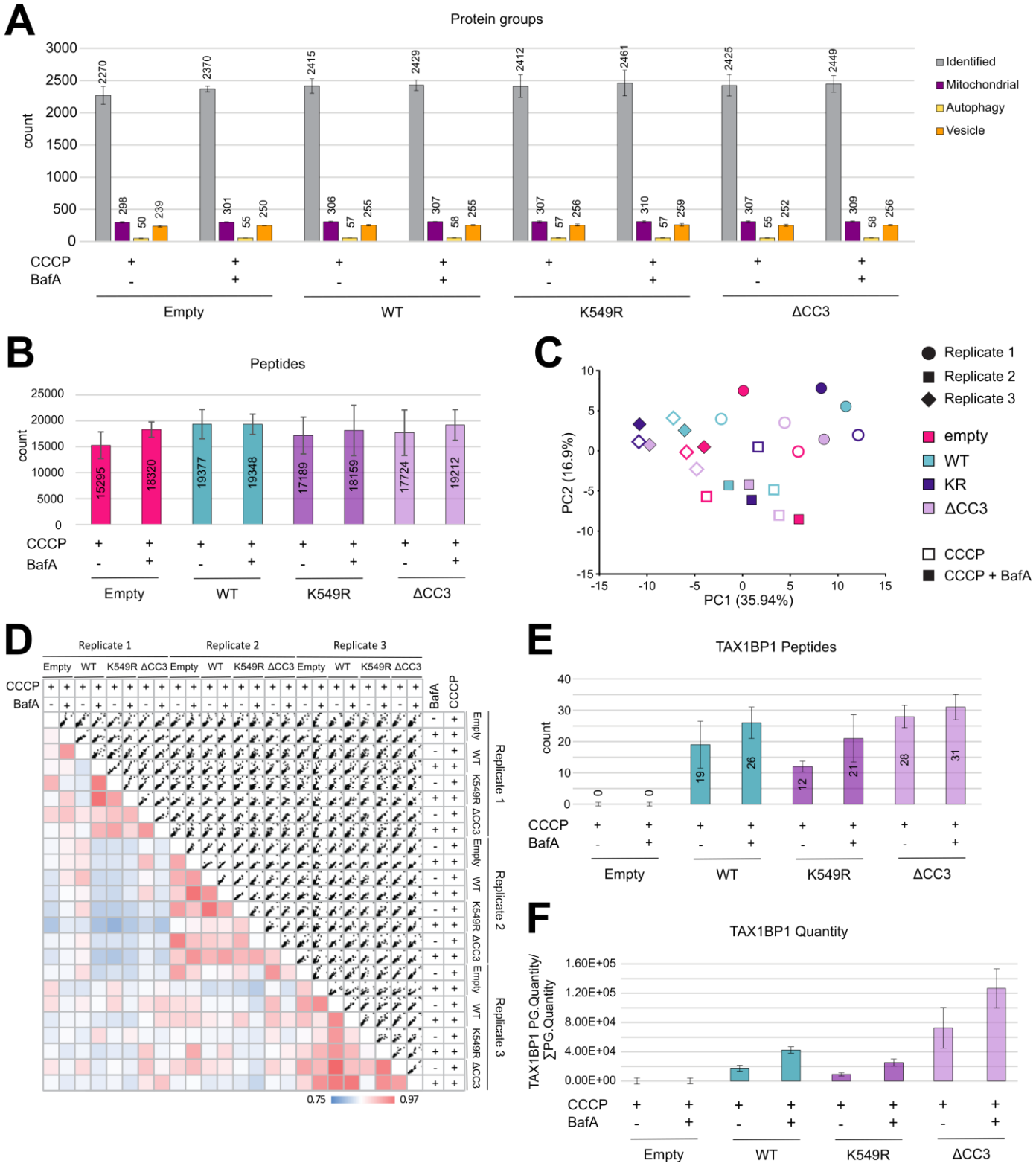
Supplementary figure 5: Characterization of small TAX1BP1-positive vesicles carrying matrix mitrochondrial material upon autophagy flux inhibition in 5KO-PARK. (A-D) Representative images of 5KO-PARK HeLa cells showing small TAX1BP1/HSP60-positive structures (magenta, cyan) positive for the indicated markers (yellow): LC3B (A), RAB7 (B), VPS35 (C) and CD63 (D). Scale bars: 5 μm.

Supplementary Figure 6



Supplementary figure 6: Characterization of TAX1BP1-positive vesicles in WT-Parkin HeLa cells after transient knockdown and re-transfection. (A) Protein expression of classical mitophagy associated autophagy adaptors in WT-Parkin and 5KO-PARK HeLa cells. Representative images of two independent biological replicates (n=2). **(B)** Example image of the CellProfiler-based identification of big (double arrowheads), intermediate (thick arrowheads) or small (thin arrowheads) TAX1BP1 structures in WT-Parkin HeLa cells overexpressing ΔCC3-TAX1BP1 after 16h CCCP combined with BafA. Numbers in white indicate pixel area of TAX1BP1-positive big structures. **(C)** Classification of TAX1BP1-positive structures observed in WT-Parkin HeLa cells after siRNA mediated knockdown, CCCP-mediated depolarization combined with BafA treatment.

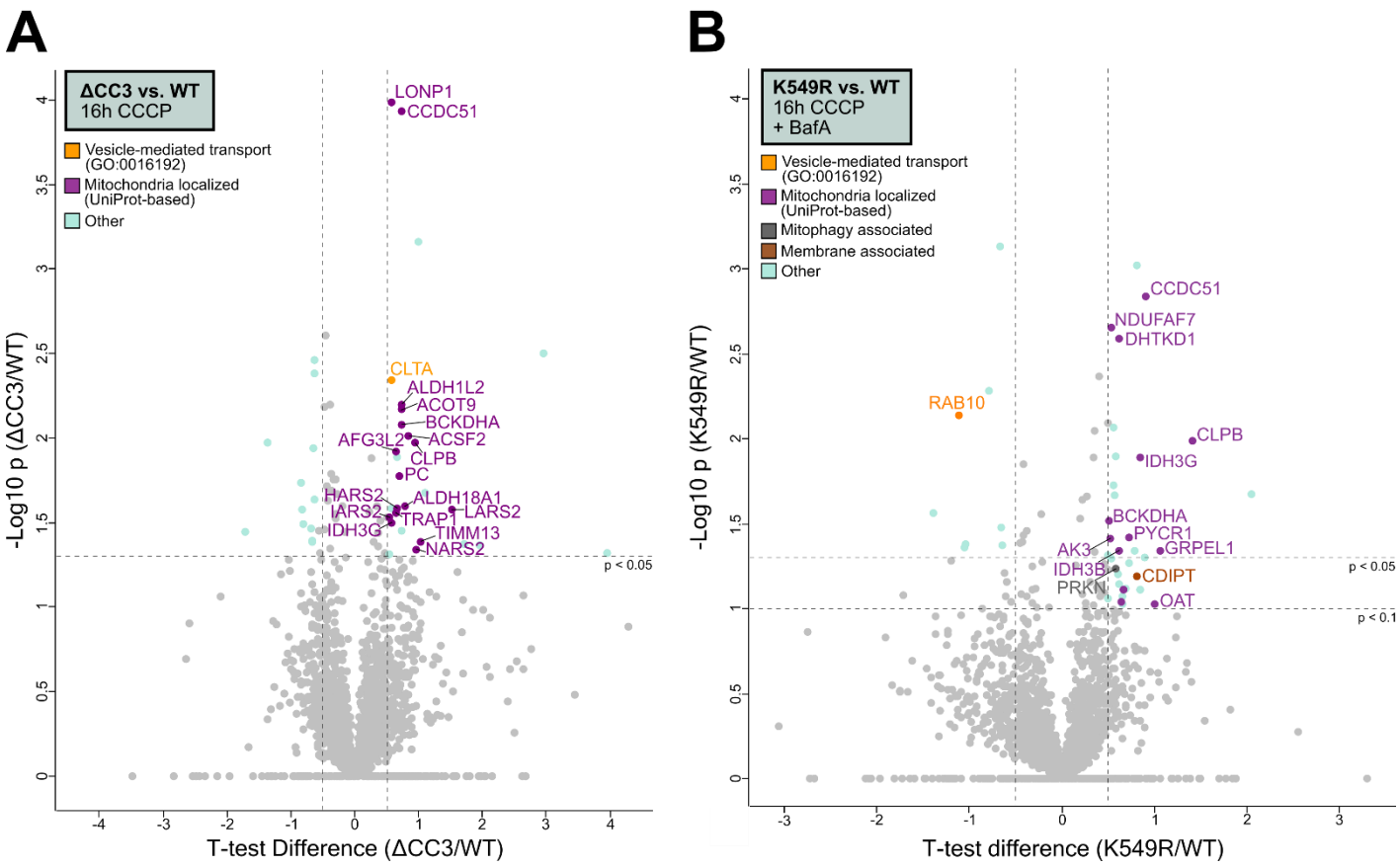
Supplementary Figure 7



Supplementary Figure 7: Quality control of the native pulldown mass spectrometry analysis. (A) Median of the number of protein groups identified per sample alongside their portion affiliated to mitochondria, the autophagy or the vesicular transport machineries. **(B)** Median of the number of peptides identified per sample. **(C)** Principal component analysis of all samples with each replicate treated individually. **(D)** Spearman rank correlation of PG Quantity with each replicate treated individually. **(E)** Median of the number of TAX1BP1

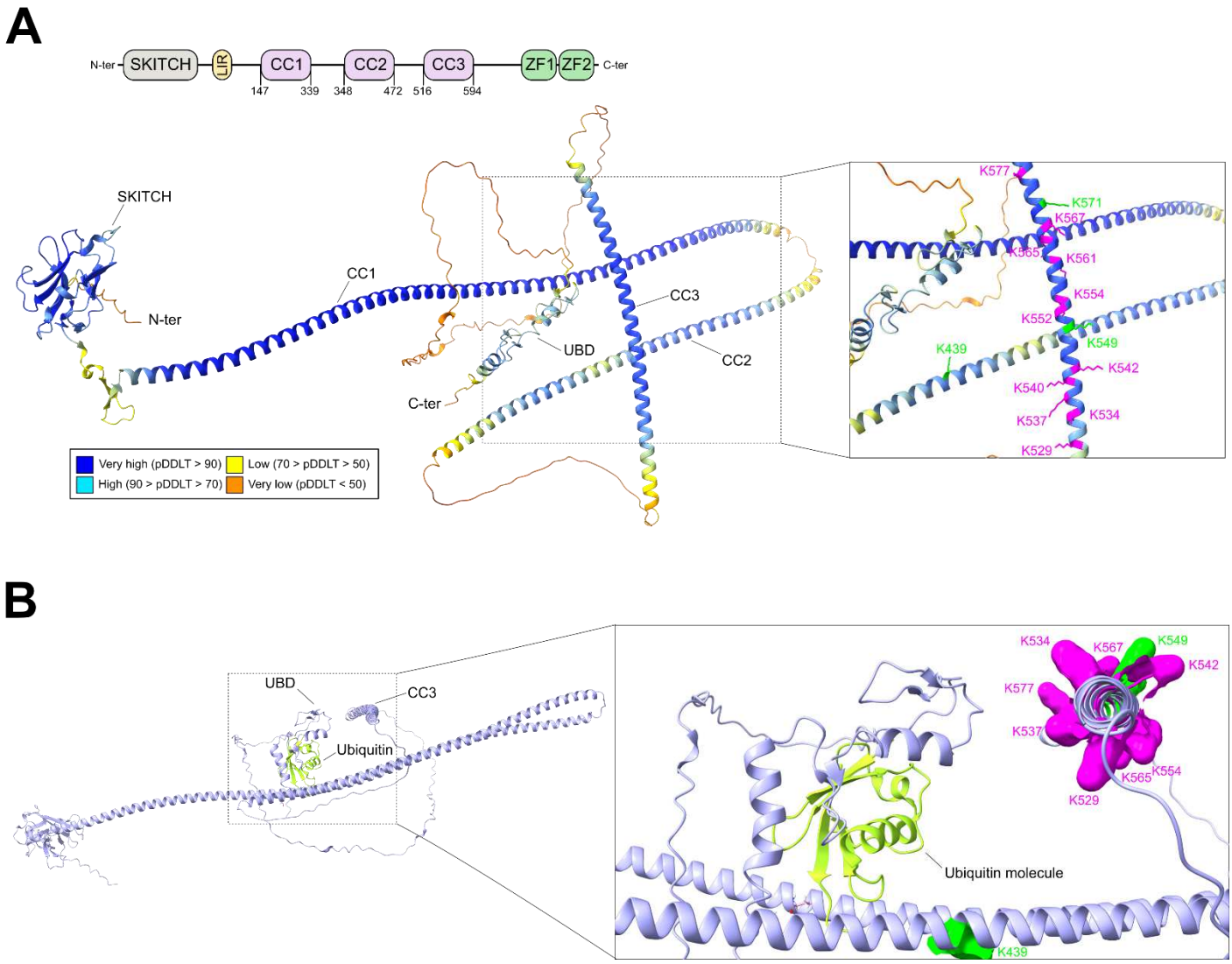
peptides per sample. **(F)** Median of the protein abundance of TAX1BP1 normalized to the total protein intensity per sample.

Supplementary figure 8



Supplementary Figure 8: Volcano plots showing ΔCC3- and K549R-TAX1BP1 after CCCP treatment only or treatment combined with BafA. (A) Statistical analysis of ΔCC3 vs. WT-TAX1BP1 after extended mitochondrial depolarization. **(B)** Statistical analysis of K549R vs. WT after CCCP treatment combined with BafA. In both cases, data are represented by the $\log_{10}$ p-value plotted against student's T-test difference. Significance lines represent p-value ≤ 0.05 and p-value ≤ 0.1, as indicated. Mitochondria localized proteins are highlighted in lila and were annotated according to UniProt. Other annotations correspond to Vesicle-mediated transport (GO:0016192) in orange, proteins related to mitophagy (gray) or proteins associated with membranes (brown).

Supplementary figure 9



Supplementary Figure 9: Structural visualization of TAX1BP1 using the predicted Alphafold structure. (A) Domain organization of the coiled-coil domains of TAX1BP1 according to Alphafold structure (top panel). Predicted Alphafold structure of TAX1BP1 with the indicated per-residue model confidence scores (pLDDT). In the zoom panel, identified lysines in the mass-spectrometry screen are highlighted in green. Highlighted in magenta are the remaining lysines of the CC3, which were not identified via MS. (B) TAX1BP1, structure in combination with an ubiquitin molecule at its ubiquitin-binding domain (UBD). Zoom panel shows lysines of CC3 (residue surface) in close proximity to the UBD. Highlighted lysines of CC3 are shown in green, if they were identified in the mass-spectrometry screen. The rest of lysines from CC3 are shown in magenta. Images created with ChimeraX (Meng *et al.*, 2023).

Supplementary Files

This is a list of supplementary files associated with this preprint. Click to download.

- SupplementaryTablesproteomics.xlsx